



TÉCNICO
LISBOA

Evaluation of the Radiosensitizing Capabilities of Target-Specific Gold Nanoparticles in the Radiotherapy of Prostate Cancer

Ana Sofia Marques

Thesis to obtain the Master of Science Degree in

Physics Engineering

Supervisor(s): Ana Belchior, PhD
Teresa Pinheiro, PhD

Examination Committee

Chairperson: Prof. Full Name
Supervisor: Prof. Full Name 1 (or 2)
Member of the Committee: Prof. Full Name 3

December 2020

Acknowledgments

This work was developed in the framework of NANOGLIO (PTDC/MED-QUI/29649/2017), funded by Fundação para a Ciência e Tecnologia (FCT, Portugal), and the TOF-PET FOR PROTON THERAPY (TPPT) project, funded by FCT and ANI (045904).

Foremost I would like to thank my supervisor, Ana Belchior, for the support through the entire thesis and for the opportunity to develop this work in a multidisciplinary research environment. I would also like to acknowledge my co-supervisor Teresa Pinheiro for the promptness and availability to answer any questions I had. A special thank you should be addressed to Fernanda Marques for all of the help in the cell culture procedures, irradiations and discussion of the results.

I would like to thank the investigators from the Radiopharmaceutical Sciences Group at C2TN for the fabrication of the gold nanoparticles used in the experimental part of the thesis and specifically to António Paulo and Francisco Silva for the assistance provided in this area. I want to extend these thanks to the group from the Metrology Laboratory of Ionising Radiation for allowing me to use their irradiation facilities and for their help with the irradiations. I also want to express my gratitude to Pedro Santos for the tireless support with the Co-60 irradiations and for answering all of my doubts about the procedure and the irradiator. Furthermore I would like to acknowledge Salvatore Di Maria for all the help with the Monte Carlo simulations and the availability to answer any questions, as well as Jorge Borbinha for the time spent teaching me how to use PENELOPE. I would like to show my appreciation to Antonella for the help with the simulations and the opportunity to discuss them, and to the Radiation Protection and Safety Group for welcoming me and assisting me through the course of this thesis.

To every colleague and professor I met in these five years, with whom I shared many memories that I will take with me.

To Patrícia, for the friendship and support in all the years we have known each other. To my family, always supportive and understanding. I would like to mention my uncles Luís and Alice, my cousin Rodrigo and my grandmother Maria. Finally, to my sister Joana for never failing to make me laugh and brightening up my day. To my parents, Cristina and Francisco, for the inspiration, for always being present and for providing me with all the resources I needed to achieve my goals. These past five years would have been a lot harder without all of this continued support and belief in me.

Resumo

O cancro é a segunda cause de morte mais comum no mundo. Um dos tratamentos mais usados para esta doença é a radioterapia, que consiste na deposição de energia nos tecidos causando danos nas células. No entanto, a radiação atingirá não só as células tumorais, mas também as células vizinhas saudáveis que irão igualmente sofrer danos. Estes danos podem ser reduzidos com o uso de radiosensibilizadores, como nanopartículas de ouro, que aumentam a energia depositada nos tecidos cancerígenos mas mantém constante a energia depositada nas restantes células.

Esta tese estudou este efeito através de trabalhos computacionais e experimentais, para raios-X e raios gama de Co-60. O programa de Monte Carlo PENELOPE foi o usado para entender melhor os parâmetros que influenciam este efeito, como o tamanho das nanopartículas, o tipo de radiação e a largura do feixe. Procedimentos *in vitro* foram também realizados em células de cancro da próstata de modo a quantificar este efeito e verificar a sua evolução com o tempo, como os ensaios de micronúcleos, MTT e clonogénicos após irradiação com raios-X (100 kVp) e raios gama de Co-60 com dois débitos de dose diferentes. Um revestimento diferente na nanopartícula foi também estudado, nomeadamente um revestimento de bombesina que se liga preferencialmente aos recetores existentes nas membranas das células do cancro da próstata utilizadas, permitindo uma maior captação celular das nanopartículas.

Os resultados mostraram que raios-X de baixa energia e débitos de dose elevados aumentam o efeito de radiosensibilização, assim como o uso de nanopartículas revestidas com bombesina.

Palavras-chave: nanopartícula de ouro, radiosensibilização, radioterapia, Monte Carlo

Abstract

Cancer is the second leading cause of death in the world. One of the most common treatments for it is radiotherapy, consisting of the deposition of energy in the tissues causing cell damages. However, the radiation will hit not only tumour cells but also healthy surrounding cells that will suffer damages. These damages can be reduced by using radiosensitizers, such as gold nanoparticles, that increase the energy deposited in the cancer tissues while keeping the energy in the rest of the cells constant.

This thesis studied this effect through computational and experimental work for both X-rays and Co-60 gamma rays. The Monte Carlo software PENELOPE was used to understand better the parameters influencing this effect, like the nanoparticle size, the type of radiation, and the beam width. In vitro procedures were performed in prostate cancer cells to quantify this effect and verify its evolution with time, such as micronuclei, MTT, and clonogenic assays after irradiation with 100 kVp X-rays and Co-60 gamma rays at two different dose rates. A different coating in the nanoparticle was also studied, specifically a bombesin coating that preferentially binds to the receptors existing in the prostate cancer cells used, allowing for a higher cellular uptake of the nanoparticles.

The results showed that low-energy X-rays and high dose rates increase the radiosensitization effect, as well as the use of bombesin-coated nanoparticles.

Keywords: Gold nanoparticle, radiosensitization, radiotherapy, Monte Carlo

Contents

Acknowledgments	iii
Resumo	v
Abstract	vii
List of Tables	xiii
List of Figures	xv
Nomenclature	xvii
1 Introduction	1
1.1 Motivation	1
1.2 Objectives	2
1.3 Thesis Outline	2
2 Theoretical Background	5
2.1 Cancer Biology	5
2.1.1 Cancer Treatment	6
2.2 Biological Effects of Radiation	8
2.2.1 Mechanisms of Cell Death	8
2.3 Interaction of Radiation with Matter	9
2.3.1 Interaction of Photons with Matter	10
2.3.2 Interaction of Charged Particles with Matter	12
2.4 Physical Quantities	13
2.5 Gold nanoparticles	14
2.5.1 Properties of NPs	15
2.6 Chemical Aspects	16
3 Materials and Methods	17
3.1 Cell Culture	17
3.2 Gold Nanoparticles	17
3.3 Irradiations	19
3.3.1 Precisa-22 Co-60 gamma rays	19
3.3.2 Eldorado 6 Co-60 gamma rays	21
3.3.3 X-rays	21

3.4	Clonogenic Assay	23
3.4.1	Procedure for clonogenic assay	24
3.5	Cytokinesis-blocked Micronucleus Assay	24
3.5.1	Procedure for the cytokinesis-blocked micronuclei assay	25
3.6	MTT assay	26
3.6.1	Procedure for the MTT assay	26
3.7	Summary of the performed experiments	27
4	Monte Carlo Simulations	31
4.1	PENELOPE	31
4.1.1	User-defined files	31
4.1.2	PenEasy	32
4.1.3	Interaction forcing	33
4.1.4	Secondary Particle Equilibrium	33
4.2	MATLAB	34
4.3	Simulations performed	34
4.3.1	Variation of the distance between the NP and the source	34
4.3.2	Variation of the NP size and beam width	36
4.4	Simulation with several NPs	36
4.5	Simulation of the experimental conditions	37
4.5.1	Co-60 irradiation	39
4.5.2	X-rays irradiation	40
5	Results	41
5.1	Dose rate uniformity with Precisa-22	41
5.2	Experiments without gold nanoparticles	42
5.2.1	Clonogenic assay results	42
5.2.2	CBMN assay results	43
5.3	Experiments with gold nanoparticles	44
5.3.1	CBMN assay results	44
5.3.2	MTT assay results	47
5.3.3	Clonogenic assay results	48
5.4	Monte Carlo simulations	50
5.4.1	Variation of the distance between the NP and the source	50
5.4.2	Variation of the NP size	51
5.4.3	Simulations with several NPs	53
5.4.4	Simulations with the experimental conditions	54

6 Discussion and Conclusions	57
6.1 Discussion of results	57
6.1.1 Comparison between Co-60 gamma rays and X-rays	57
6.1.2 Comparison between AuNPs and BBN-AuNPs	59
6.1.3 Comparison between dose rates	59
6.2 Comparison between experimental and computational work	60
6.3 Conclusions	61
6.4 Future Work	62
Bibliography	63

List of Tables

3.1	Radiation sources and respective dose points and dose rates.	28
5.1	Results on the variation of the distance between the source and the NP	52
5.2	DEF in the nucleus and in the cytoplasm with varying NP sizes.	53
5.3	Ratio between the energy deposited by electrons on each shell for the gold simulation and the water simulation. The small beam corresponds to a width of 1 μm and the large beam to a width of 5 and 50 μm for Co-60 and X-rays, respectively.	55

List of Figures

2.1	Formation of cancer	6
2.2	DNA strand breaks	9
2.3	Photon interactions.	11
2.4	De-excitation processes.	12
2.5	Mass attenuation coefficients	15
3.1	Chemical structure of the coatings used on the AuNPs for this thesis. Illustrations taken from [34].	18
3.2	AuNP-TDOTA characterization	18
3.3	BBN-AuNP-TDOTA characterization	18
3.4	Gold concentration study	19
3.5	Precisa-22 chamber	20
3.6	Ionization chamber	20
3.7	Support for dose rate measurements	21
3.8	Co-60 irradiation setup	22
3.9	X-rays irradiation setup	22
3.10	X-rays spectrum.	23
3.11	Survival curves	23
3.12	Colonies	25
3.13	Example of groups of cells not considered colonies	25
3.14	Example of image from CBMN assay	26
3.15	Example of image from MTT assay	27
3.16	Summary of the experimental procedures	29
4.1	Geometry of the validation simulation	35
4.2	Spectra used in the validation simulations.	35
4.3	Geometry of the study of NP size	36
4.4	Geometry of the study with several NPs.	37
4.5	Geometry of the final simulations	39
5.1	Dose rates in the wells of one quarter of each cell culture plate. All values are in Gy/min.	41

5.2	Layout of the samples in culture plates. The blue corresponds to the wells containing cells. The remaining wells were empty.	42
5.3	Clonogenic assay results without NPs	42
5.4	Residuals from survival curve	43
5.5	CBMN assay results without NPs	44
5.6	CBMN assay results	45
5.7	Cells without micronuclei	45
5.8	Cells with 1 micronucleus	46
5.9	Cells with 2 micronuclei	46
5.10	Cells with 3 micronuclei.	47
5.11	MTT assay results	48
5.12	MTT assay results	48
5.13	Clonogenic assay results	49
5.14	Photo of clonogenic assay	50
5.15	Photo of clonogenic assay	51
5.16	DEF variation with NP size and beam width.	52
5.17	Energy deposited outside of the NP	53
5.18	Variation of DEF with distance for X-rays.	54
5.19	Variation of DEF with distance for Co-60.	55

Nomenclature

AuNP Gold nanoparticle

BBN Bombesin

BN Binucleated

CBMN Cytokinesis-blocked Micronucleus

DEF Dose enhancement factor

DNA Deoxyribonucleic acid

DSB Double-strand break

EBRT External beam radiotherapy

EPR Enhanced permeability and retention

IMRT Intensity-modulated radiotherapy

LET Linear energy transfer

NP Nanoparticle

RBE Relative Biologic Effectiveness

ROS Reactive oxygen species

SSB Single-strand break

A Mass number

Z Atomic number

Chapter 1

Introduction

1.1 Motivation

Cancer is the second leading cause of death in the world and it was responsible for an estimated 9.6 million deaths in 2018. [1] In Portugal, about 24.6% of all deaths in 2018 was due to cancer. [2] Specifically, prostate cancer is the second most commonly occurring cancer in men worldwide and the fourth most commonly occurring cancer overall. [3]

Cancer is a large group of diseases involving modifications in the genome affected by interactions between the host and the environment. Typical characteristics of cancer are uncontrolled replication and the capacity to penetrate in other tissues, known as metastasis. Currently, the most widely used treatment modalities are surgery, chemotherapy, immunotherapy and radiotherapy. The selection of treatment depends on the type of cancer, its locality and stage of progression.

Cancer surgery consists on the removal of tumour tissues during an operation by a surgeon. It is the method that assures least damage to the surrounding healthy tissues, however often it is not possible for the surgeon to remove the entire tumour and so it is combined with other therapies. Chemotherapy uses drugs that target the cancer cells and stop tumour progression by killing off their ability to divide and inducing cell death. However, chemotherapeutic drugs also target normal cells, resulting in several side effects. Immunotherapy is defined as the treatment of diseases by manipulating the immune system, stimulating it to fight infections. [4]

Finally, radiotherapy consists on the deposition of energy in the cancer cells by irradiation (gamma rays, X-rays, electrons, protons or ions). The irradiation causes damages to the cancer cells themselves or their vasculature and thus cause cell death or nutrient starvation. [5] However, it is not possible to irradiate only the tumour cells, surrounding healthy tissue will also receive a considerable dose, because the mass energy absorption properties of cancer and healthy tissues are very similar. [6] It is therefore necessary to reduce the radiation dose delivered to the healthy tissues of the patient, while maximizing the dose delivered to the tumour. This ratio between the treatment efficacy and the side effects is called the therapeutic index. To increase this ratio, we can use the following procedures, among others:

- Decrease the resistance to radiation of the tumour tissues;

- Increase the resistance to radiation of the healthy tissues;
- Increase the radiosensitization of the tumour.

Hence one way to maximize the dose delivered to the tumour is the use of radiosensitizers, which are defined as materials able to make tumour cells more sensitive to radiation. Metal-based nanoparticles represent an attractive option, as they absorb more energy per unit mass than soft tissue, increasing the local dose deposited in the tumour. [6] Specifically, gold nanoparticles (AuNPs) have several advantages, such as low cytotoxicity and effectiveness in dose enhancement. [5]

1.2 Objectives

The aim of the work is to determine the potential benefit of combining radiation treatment with AuNPs, by studying the effects induced by radiation: gamma- and X-rays in prostate cell lines loaded with AuNPs. The cancer cell line that will be used is PC3 (prostate tumour).

For this, both experimental and computational work has been developed. First, the cells were irradiated with Co-60 gamma rays for several dose points to obtain a survival curve. Afterwards, a specific dose was chosen for the cells to be irradiated with Co-60 and X-rays in the presence of AuNPs, and the induced damages were studied, through clonogenic, micronucleus and MTT assays. Finally, a comparison between the effects induced by the AuNPs for two different dose rates is presented for Co-60 irradiation.

For the simulation work, the Monte Carlo code used was PENELOPE (PENetration and Energy Loss of Positrons and Electrons). This software allowed for the estimation of the dose enhancement, a better understanding of this effect, and a confirmation of the experimental results.

1.3 Thesis Outline

This thesis is divided into six chapters.

After this first introductory one, the second chapter is the theoretical background for the developed work. It contains an overview on the interaction of radiation with matter, the most important physical and dosimetric quantities for this work and a section on gold nanoparticles and its properties. Also included is a summarized view of cancer biology and the most common cancer treatments currently used, as well as the biological effects of radiation.

The third chapter mentions the materials and methods used in the experimental part of the thesis, such as the irradiation setups the assays performed with the cells and the characterization of the nanoparticles used.

In chapter 4, there is a generic explanation of Monte Carlo methods, a specific description of PENELOPE and the simulations that were developed, including the geometries and materials used.

The fifth chapter contains the results of the thesis, both experimental and computational, including the experiments with and without nanoparticles and all the assays performed.

The final chapter is the conclusion of the work, consisting on not only comparing the results of the assays but also combining the experiments with the simulations. A section on ideas for future work is also included.

Chapter 2

Theoretical Background

In this chapter, several important concepts are described, starting from cancer biology and the biological effects of radiation. The physical processes that occur when charged and uncharged particles interact with a medium are briefly discussed and the effects of radicals and other reactive species formed as a consequence of irradiation are also described.

2.1 Cancer Biology

As mentioned before, cancer is a disease defined by uncontrolled growth and spread to other tissues. The most lethal cancers start in the lung, colon, and breast (for women) or prostate (for men). For a cancer cell to be created, there must be a mutation in one gene of a normal cell followed by a series of mutations in other genes in this original cell's clonal descendants, as seen in figure 2.1.

The cancer phenotype is characterized by uncontrolled cell proliferation, genomic instability, immortality and the ability to disrupt not only local but also distant tissues. [7]

- Uncontrolled Cell Proliferation:
 - Normal cells divide due to signals from adjacent cells. Cancer cells, on the other hand, make their own stimulatory signals.
 - Normal cells cease to grow when they come into contact with other cells, unlike cancer cells that keep growing.
 - Normal cells die via apoptosis, while cancer cells are resistant to apoptotic signals.
- Genomic Instability:
 - Normal cells repair any damage to the DNA, while cancer cells are defective in repairing this damage and allow mutations to accumulate.
- Cellular Imortality:
 - Normal cells do not divide indefinitely, while cancer cells have lost this characteristic. The telomeres shorten with each cell division process until the cells can no longer divide. However,

cancer cells express the enzyme telomerase, causing them to maintain the telomere length even after many divisions.

- Tissue Invasion:
 - Normal cells stay within their respective tissues. Cancer cells invade the surrounding tissue and can even infiltrate the bloodstream, traveling to more distant organs. Metastasis produces secondary tumours responsible for 90% of cancer deaths.
 - Cancer cells can generate new blood vessels that provide nutrients and routes for it to metastasize.

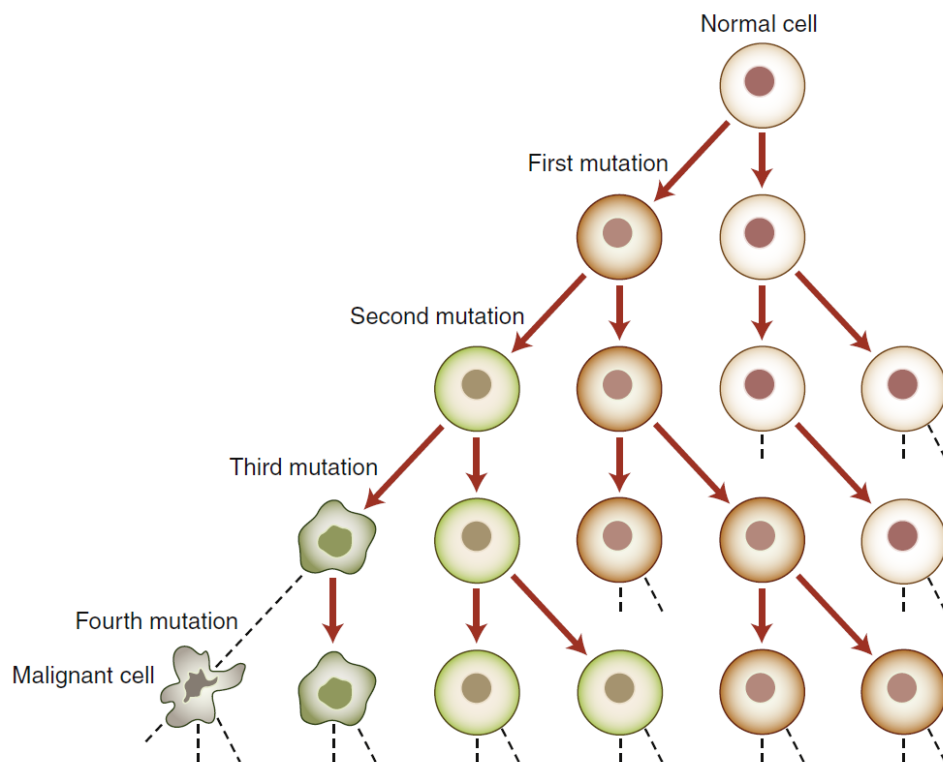


Figure 2.1: Formation of a malignant cell through a series of mutations. Illustration taken from [7].

2.1.1 Cancer Treatment

The most common cancer treatment modalities are surgery, chemotherapy, radiotherapy and immunotherapy.

Surgery

Surgery is the most conventional treatment of tumours. It is one of the modalities that assures least damage to the healthy cells surrounding the cancer tissues. A surgery in cancer therapy can have several goals, depending on the stage of the cancer: the removal of the entire tumour, the debulking of

the tumour in cases where removing the entire tumour can cause damages to nearby tissues and the mitigation of cancer symptoms. [8]

Chemotherapy

Chemotherapy stops the progression of tumours by affecting their ability to divide and enforcing apoptosis. However, chemotherapeutic drugs also target healthy cells, resulting in several side effects, such as hair loss, nausea, fatigue, vomiting, etc. Additionally chemotherapy patients can also become immunocompromised, which may lead to infections and ultimately death.

Currently there are more than 100 drugs used in chemotherapy with different chemical structures, that can be used alone or in combination therapies. [8]

Immunotherapy

Immunotherapy consists on the use of components of the immune system, such as antibodies, to treat diseases. Specifically in cancer treatment, it aims to destroy the tumor cells or to aid the immune system of the patients to do it.

Antibodies recognize and eliminate pathogens but they can be deliberately generated to recognize different target molecules, like tumour markers, bacteria or hormones. They can provide specificity and lower toxicity in cancer treatment.

Newer treatment possibilities include immunoconjugates, which are antibodies linked to cancer-killing agents such as drugs or radioisotopes. The antibodies would lead the agent to the cancer cells and they would act to kill the tumour, while lowering the damage to healthy cells. [9]

Radiotherapy

Radiotherapy can be divided in two categories: external beam radiotherapy (EBRT) and brachytherapy. In the latter, a radioactive source is placed inside the body, directly into the tumour or very close to it. This allows for a very high dose to be delivered more precisely to the cancer, decreasing the dose that healthy tissues will receive. [10]

Ionizing radiation can be used to kill the cancer cells. External beam radiotherapy is based on the fact that cells with damaged DNA are unable to replicate and therefore cell division is halted. However, as mentioned in section 1.1, neighbouring healthy cells will also be targeted and damaged.

Common EBRT techniques include fractionation and intensity-modulated radiation therapy (IMRT), among others. IMRT is a technology that uses a three-dimensional reconstruction of the tumour to modulate the intensity of the radiation beam to deliver different doses to the cancer and to nearby organs.

Fractionation is the process of dividing a dose of radiation into fractions, in order to maximize the destruction of cancer cells and minimize the damage to normal tissues. [8] There are several advantages in using this technique:

- Redistribution: the radiosensitivity of a cell depends on their stage in the cell cycle. Malignant cells are at different points in this cycle and therefore, delivering the total dose into multiple fractions increases the probability of irradiating cells when they are the most radiosensitive.
- Re-oxygenation: when tumour cells are hypoxic, they are less susceptible to the indirect effects of radiation because there is less ROS production. Cells are only hypoxic for a certain period of time, therefore dose fractionation allows the cells to improve their oxygen supply in the intervals between fractions and consequently become more radiosensitive in the next doses.
- Repair: Healthy cells have a greater ability to repair DNA damage than tumour cells. Splitting the total dose into fractions gives healthy cells an opportunity to repair the damages between fractions, while malignant cells are less able to recover from the damage. [11]

2.2 Biological Effects of Radiation

According to several experiments, DNA is the main target for radiation-induced biological effects. Therefore, the most used method for determining the efficacy of radiotherapy is to monitor the amount of DNA damage, namely the number of strand breaks produced.

Deoxyribonucleic acid (DNA) is a large molecule with a double-helical structure, consisting of two strands held together by hydrogen bonds. The backbone of each strand consists of alternating sugar (deoxyribose) and phosphate groups. Attached to this backbone are four bases, the sequence of which specifies the genetic code; these are thymine, cytosine, adenine and guanine.

Radiation can induce a large number of lesions in the DNA molecules, however most are repaired by the cell. The typical damages include strand breaks (single and double) and base damages. Single-strand breaks (SSBs) and double-strand breaks (DSBs) are represented in figure 2.2. When the damages take place in one single strand of the DNA or in both strands but with breaks well separated, the cell can repair these lesions by taking the opposite strand as a template. However, when these damages occur in both strands and the distance between them is small, it can result in cleavage of the chromatin into two separate pieces. [12]

DSBs are considered the most important lesions produced in chromosomes by radiation. However, radiation can lead to complex DNA damage, with multiple non-DSB lesions forming a clustered DNA damage. Since this clustered DNA damage may require prolonged activation of repair systems, it is usually associated with an incomplete repair of damaged sites and therefore an increase in mutation rates. Clustered DNA damages and DSBs induced by radiation can then cooperatively contribute to cell death. [14]

2.2.1 Mechanisms of Cell Death

For cells cultured *in vitro*, death is defined as the loss of reproductive integrity, i.e., cells are considered dead if they cannot divide indefinitely and form colonies. A survivor that has retained its reproductive integrity and is able to proliferate to produce a large clone is said to be clonogenic.

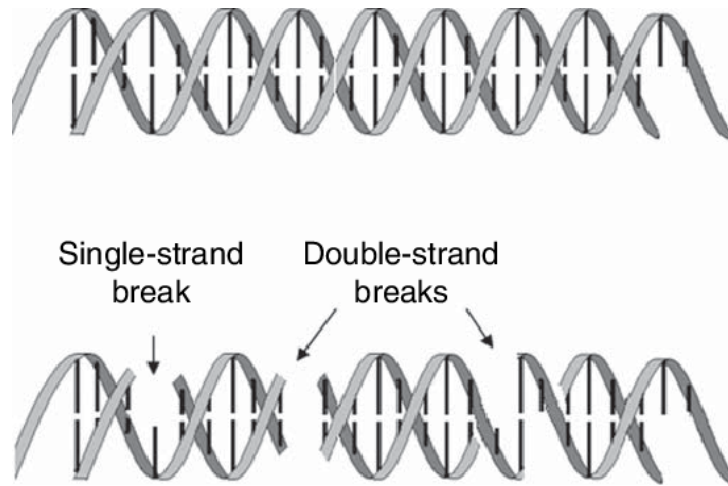


Figure 2.2: Representation of the DNA without damages (on top) and with strand breaks. Illustration taken from [13].

Cells may die by different mechanisms. When considering irradiation, it is relevant to mention apoptotic, mitotic and autophagic death.

Apoptosis, or programmed cell death, is a process in which cells die in a controlled way. It is considered a vital component of various processes including normal cell turnover, proper development and functioning of the immune system, embryonic development and chemical-induced cell death. Apoptosis is characterised by a series of characteristic morphological changes in the cell, along with a number of enzyme-dependent biochemical processes, leading to the clearance of cells from the body, with minimal damage to surrounding tissues. This mechanism of cell death can be initiated by the cell itself when it detects damages (intrinsic pathway) or it can result from the interaction between a cell of the immune system and a damaged cell (extrinsic pathway of apoptosis). Apoptosis occurs in normal tissues, as described previously, but it can also be induced in some tumors by radiation. Another common form of cell death from radiation is mitotic death, when cells die attempting to divide because of damaged chromosomes. [15] This is a form of delayed reproductive death.

A third process that should be mentioned is autophagy. Autophagy is a process of metabolic recycling, and involves the self-digestion of subcellular organelles and molecules associated with lysosomes. Cytoprotective autophagy in cancer cells limits the radiotherapy's efficacy, because it includes the removal of radiation-damaged organelles and molecules, giving cancer an opportunity to survive radiation-induced damage. [16]

2.3 Interaction of Radiation with Matter

Radiation can be divided into two categories: ionizing and non-ionizing, depending on its ability to ionize atoms. For radiotherapy purposes, only ionizing radiation is of interest. It is also useful to separate this type of radiation into directly ionizing and indirectly ionizing, to emphasize the differences between the interactions of charged and uncharged particles with matter. Directly ionizing radiation refers to charged particles, which deliver their energy to matter directly. In contrast, indirectly ionizing radiation refers to X-

or gamma-ray photons or neutrons that first transfer their energy to charged particles along their track, and then these charged particles, in turn, deliver energy to matter. There are several physical processes possible when energetic particles interact with matter.

2.3.1 Interaction of Photons with Matter

There are essentially five types of interactions X- and gamma-ray photons can have with matter: photoelectric effect, Compton scattering, pair production, Rayleigh scattering and photonuclear interactions. The first three interactions are the most important because they result in the transfer of energy to matter. Rayleigh scattering is an elastic process and photonuclear interactions are only significant for photon energies above a few MeV, where they may produce neutrons. [17]

Photon interactions are characterized statistically by their probability, depending on the specific medium traversed and on the photon energy.

The photoelectric effect consists of the absorption of the incident photon, followed by the emission of an electron from the target atom. This ejected electron will have a kinetic energy (E_K) equal to the energy of the incident photon (hf) minus the binding energy of the orbiting electron shell in the material (E_B):

$$E_K = hf - E_B \quad (2.1)$$

The probability of this process is strongly dependent on the atomic number Z and the energy hf of the photons. It is largest for high- Z materials and low-energy photons, varying as $Z^4/(hf)^3$.

The Compton effect refers to the scattering of the incident photon and the emission of an electron. In this case, the kinetic energy acquired by the electron is given the following equation, where hf is the incident photon energy and θ is the angle at which the photon is scattered:

$$E_K = hf \frac{1 - \cos(\theta)}{\frac{mc^2}{hf} + 1 - \cos(\theta)} \quad (2.2)$$

Pair production occurs when the incoming photon is converted into an electron-positron pair, only possible when the photon has an energy larger than $2mc^2$. The distribution of the excess energy between the electron and the positron is continuous, that is, the kinetic energy of any of these particles can vary from 0 to a maximum of $hf - 2mc^2$. Pair production becomes more probable with increasing photon energy and it depends on the atomic number approximately as Z^2 . [18]

For each material, the photoelectric effect is predominant for lower energies, the Compton scattering for intermediate energies and, finally, pair production for the highest energies. In image 2.3, there is a scheme of 4 interactions of photons with matter including the three main ones mentioned before and also coherent (or Rayleigh) scattering.

After the atoms of the material are excited or ionized, they can de-excite through the emission of fluorescent photons or Auger electrons. [20] For high- Z materials such as gold, the emission of fluorescent photons is favored over Auger electron emission [18]. Auger electrons can however deliver a relatively

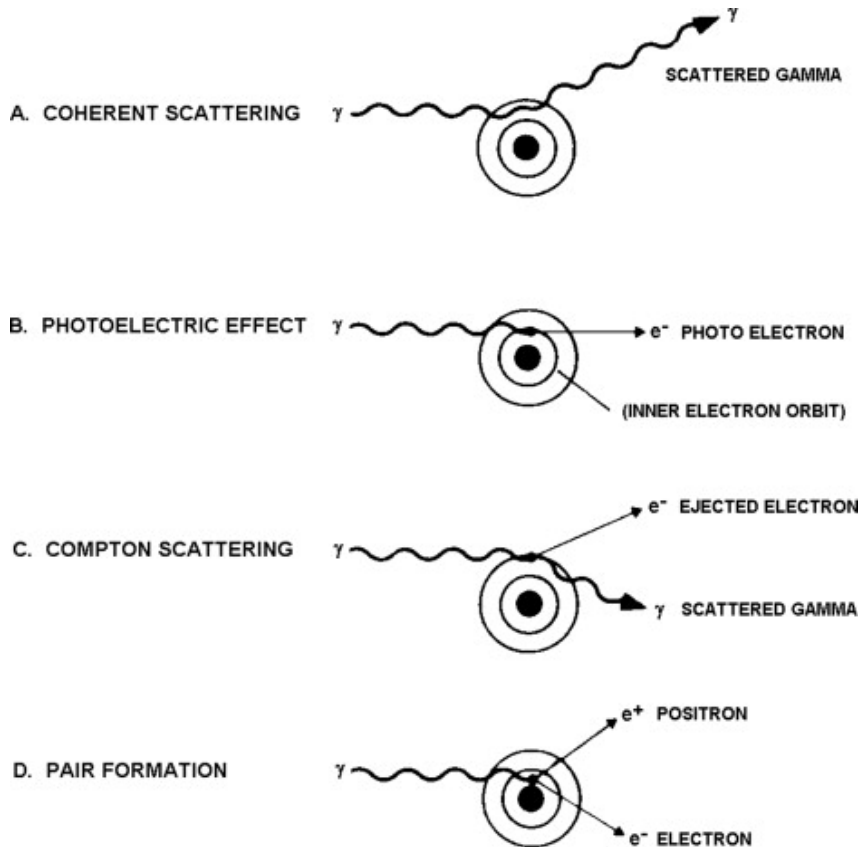


Figure 2.3: Image of the most important interactions of photons with matter: coherent scattering, photoelectric effect, Compton scattering and pair production. Illustration taken from [19].

high local dose, while fluorescent photons can travel farther in the tissue, causing a delocalization of the dose (typical attenuation lengths are in the order of the cm). [21] The Auger effect is then a physical phenomenon in which the filling of an inner-shell vacancy of an atom is accompanied by the emission of an electron from the same atom. For high-density media, Auger electrons have a typical range lower than 10nm. This Auger electron will propagate through the system, causing several secondary ionizations. [22] These de-excitation processes are illustrated in figure 2.4. First, photoelectric effect occurs and a photoelectron is emitted with an energy $E - \Phi$, where E is the original photon energy and Φ is the binding energy of this electron in its shell, in this case K-shell (Φ_K). Afterwards an electron from a shell with a lower binding energy will fill in the vacancy created, in this case from the L-shell. The difference in the binding energies is given off as a fluorescent photon or an Auger electron. [23]

An important parameter when discussing photons travelling through a medium is the linear attenuation coefficient μ , which is the probability per distance travelled that a photon interacts by any process, having the dimensions of m^{-1} (or the most common unit of cm^{-1}). The mass attenuation coefficient μ/ρ is obtained by dividing μ by the density of the material (usually expressed in cm^2g^{-1}). This parameter depends on the photon energy and on the material, representing the probability of an interaction per $g\ cm^{-2}$ of material traversed.

The mass-energy absorption coefficient, (μ_{en}/ρ) , on the other hand, is a measure of the amount of incident photon energy transferred to kinetic energy of the charged particles. In contrast to the mass

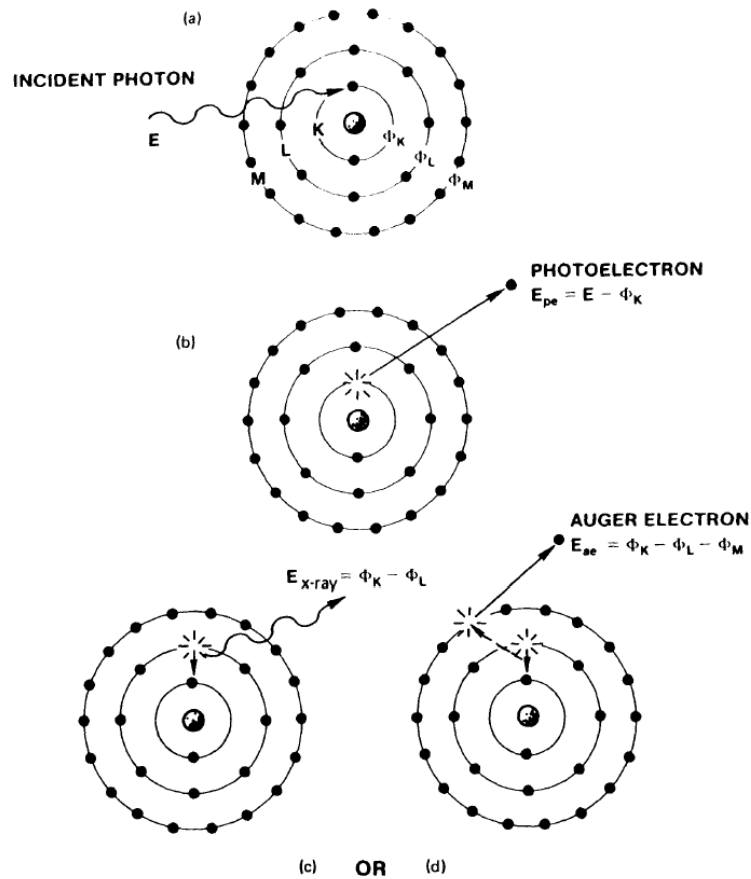


Figure 2.4: Diagrams of the de-excitation processes Auger effect and fluorescence emission. Illustration taken from [23].

attenuation coefficient, related to the average number of interactions in a medium, this quantity takes into account the fraction of the kinetic energy that is subsequently lost in radiative processes. Therefore, it is better related to the absorbed dose. [24]

2.3.2 Interaction of Charged Particles with Matter

While uncharged radiations may traverse a medium and not interact at all, a charged particle interacts with one or more electrons or with the nucleus of almost every atom it passes, due to its Coulomb electric force field. [17]

The possible energy-loss mechanisms are different for heavy charged particles or electrons/positrons. The processes enumerated will refer only to electrons/positrons ('beta particles'), as it is what is relevant for the scope of this thesis.

Beta particles can excite and ionize atoms, radiate photons by bremsstrahlung, Cherenkov radiation and transition radiation, or directly interact with the Coulomb field of the nucleus (multiple scattering). [25]

The average rate of energy loss per unit path length is the stopping power, which can be divided into collision stopping power (ionization and excitation) or radiative stopping power (bremsstrahlung).

The energy spent in radiative events is transported from the charged particle track, while that spent in collisions produces ionizations and excitations, contributing to the dose near the track. The collision stopping power depends on the particle's energy and charge, and on certain properties of the material, such as Z/A (Z and A are the atomic and mass number of the material, respectively), the material density and its mean excitation energy. The radiative stopping power is related to the particle's kinetic energy and to the ratio Z^2/A . [17]

Another important parameter is the linear energy transfer (LET), or restricted stopping power. This is given by equation 2.3, where dE_{Δ} is the average energy locally imparted to the medium by the charged particle in traversing the distance dl .

$$LET = \frac{dE_{\Delta}}{dl} \quad (2.3)$$

High LET radiation usually causes clustered damages in biological systems, while low LET radiation causes isolated lesions.

2.4 Physical Quantities

Radiation fields can be described by several nonstochastic quantities, such as the fluence and the fluence rate.

The fluence Φ is given by equation 2.4, where dN is the number of particles incident on a sphere with cross sectional area dA :

$$\Phi = \frac{dN}{dA} \quad [m^{-2}] \quad (2.4)$$

The fluence rate ϕ is the increment of fluence during the infinitesimal time interval dt :

$$\phi = \frac{d\Phi}{dt} = \frac{d}{dt} \frac{dN}{dA} \quad [m^{-2} s^{-1}] \quad (2.5)$$

To describe the interaction of such radiation fields with matter an important quantity is the absorbed dose. It is the quotient between the mean energy imparted by ionizing radiation $d\epsilon$ on a medium and its mass dm :

$$D = \frac{d\epsilon}{dm} \quad [Gy] \quad (2.6)$$

The absorbed dose rate during the time interval dt is given by:

$$\dot{D} = \frac{dD}{dt} = \frac{d}{dt} \frac{d\epsilon}{dm} \quad [Gy s^{-1}] \quad (2.7)$$

Kerma is another relevant nonstochastic quantity, used only for fields of indirectly ionizing radiations. It is defined as the expectation value of the energy transferred (ϵ_{tr}) to charged particles in a certain volume V , including radiative-loss energy but excluding the amount of energy that is passed from one

charged particle to another.

$$K = \frac{d\epsilon_{tr}}{dm} \text{ [Gy]} \quad (2.8)$$

However, equal doses of different types of radiation do not produce the same biologic effects, because at the micro and nanoscopic level, their energy deposition patterns are different. Therefore, to compare different types of radiation, a quantity called Relative Biologic Effectiveness (RBE) is used. This quantity relates a given radiation type to a standard radiation, usually X-rays. It is calculated as ratio between the dose of X-rays and the dose of the different radiation type required for equal biologic effect.

2.5 Gold nanoparticles

As mentioned before in section 1, radiosensitizers are materials that make tumour cells more sensitive to radiation. Specifically, gold nanoparticles (AuNPs) have several advantages: [5, 26]

- Good biocompatibility;
- Low cytotoxicity;
- Straightforward synthesis in a wide range of sizes;
- Effective in dose enhancement due to high atomic number ($Z_{Au} = 79$);
- Smaller than the typical pore size in leaky tumour vasculatures;
- Long circulatory half-lives;
- Can be labeled with medical radionuclides and MRI contrast agents;
- Allows for the attachment of ligands required to target cancer cells.

One of the reasons gold is chosen is because of its mass attenuation and mass-energy absorption coefficients compared with that of soft tissue (or water). As seen in figure 2.5, in the keV region, this difference can reach two orders of magnitude. Therefore, there will be more secondary electrons produced in the gold that will deposit their energy close to the NP.

Following these early ionizations/excitations, the system de-excites by a rearrangement of the electronic states. This occurs by the emission of fluorescent photons or by the emission of Auger electrons. They not only ionize the surrounding biomolecules, but also other NPs nearby, creating a cascade. [20]

The cellular uptake of AuNPs is highly dependent on the size and surface coating of the NP. One of the ways AuNPs enter tumour tissues is by the Enhanced Permeability and Retention effect (EPR). The EPR effect describes the leaky tumour vasculature that originates from its rapid growth rate. Because of this, macromolecules such as NPs tend to accumulate within tumour tissue at higher concentrations than in healthy tissue.

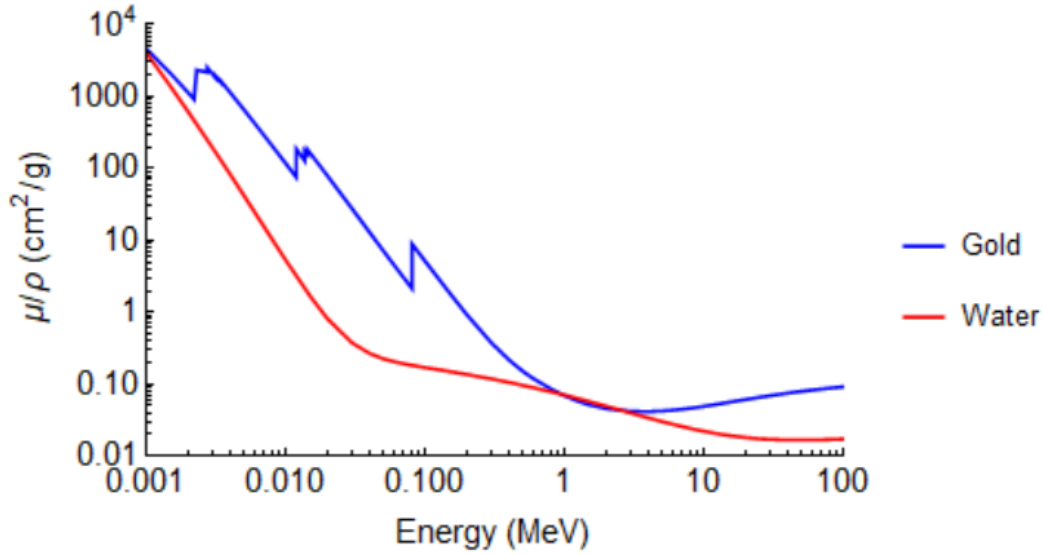


Figure 2.5: Plot of the mass attenuation coefficients for gold and water, with values taken from the NIST XCOM database. The human cell consists approximately of 70% water, so water can be considered equivalent to soft tissue.

The radiosensitization effect of NPs is quantified using the Dose Enhancement Factor (DEF), defined as the ratio between the dose absorbed by the tumour cells in the presence of the NPs and the dose absorbed in the absence of NPs. [5]

$$DEF = \frac{D_{with\ gold}}{D_{without\ gold}} \quad (2.9)$$

2.5.1 Properties of NPs

The most important parameters to consider for the use of NPs in cancer therapy is their size and surface coating. These properties will determine their uptake inside the cells, their cytotoxicity and also their interaction with the incident radiation.

Due to the EPR phenomenon, smaller NPs are more easily captured by the tumour cells, but they are eliminated faster by the body through renal clearance. This will prevent an accumulation of NPs in specific organs, but also decrease the dose enhancement effect. Regarding the interaction of the NPs with radiation, the bigger the NP the more likely it is that the secondary electrons deposit their energy inside the NP instead of the tumour cells, decreasing their radiosensitization effect.

The coating of NPs can be used to target the cancer cells, through passive or active targeting. Passive targeting is related to the EPR effect: the leaky vasculature around tumours causes a higher uptake of NPs than in healthy cells. [5] Alternatively, active targeting is based on the targeting of membrane receptors that are particularly overexpressed in cancer cells, such as the Gastrin Releasing Peptide receptors (GRPr). These receptors can be targeted with biomolecules that have high affinity towards them. Bombesin (BBN) is a peptide that can be used for this, due to its specificity towards GRPr that are overexpressed in several tumours, specifically in prostate cancers. [27]

Another field where NPs are being studied is theranostics, the combination of therapy and diagnostics. It is based on the fact that these NPs allow for other substances to be attached to them such as radioactive elements that can be used for imaging and therapy. The NP is coated with a molecule that can be labelled with the radioisotope.

2.6 Chemical Aspects

Most of the incident energy on the AuNP is actually transferred to the water surrounding it, leading to the production of radicals and other reactive species. Reactive Oxygen Species (ROS) have a short diffusion length, contributing for an increase on the local dose (similarly to Auger electrons). The highest concentration of ROS will be therefore close to the surface of the AuNPs. [28]

Reactive radicals, such as $\cdot\text{OH}$, $\text{NO}\cdot$ or $\cdot\text{O}_2^-$ or non-radical molecules such as H_2O_2 can rupture molecular bonds and oxidise the DNA (or other structures like membranes and organelles). [5] This oxidative stress is currently considered the major cause of a radiosensitization effect in the MeV range, where the photoelectric absorption has a very small cross section. [6]

ROS are continuously produced by the biological system as a result of electron leakage from the mitochondria during the Electron Transport Chain (the ETC is the main source of ATP production). However, the toxic levels of ROS are immediately detoxified by the endogenous antioxidant defense system. In case of failure of this defense system and/or overproduction of ROS, the cellular redox balance gets disrupted creating an environment of oxidative stress. This oxidative stress can cause an abnormal functioning of the cell cycle. ROS-mediated cell killing may induce death through apoptosis and permanent cell cycle arrest, among others. [29]

ROS can also affect membranes, resulting in lipid peroxidation (oxidative degradation of lipids). Lipid oxidative damage is associated with the membrane's permeability and protein/molecular transport disruptions. In addition, radiation can induce endogenous ROS production in mitochondria and alter mitochondrial membrane permeability, which in turn, further stimulates ROS production. Since repair systems are not well-developed in the mitochondria, excessive ROS generation by irradiation can contribute to extensive mitochondrial DNA (mtDNA) damage. This damage might be linked to permanent mitochondrial malfunction, causing a stimulation of the intrinsic apoptotic pathway. [16]

Chapter 3

Materials and Methods

In this chapter, there is a basic explanation of the materials and methods used in the experimental part of the thesis, including procedures for cell culture, irradiation setups and finally, a more theoretical explanation on the performed assays, such as the clonogenic, CBMN and MTT assays.

3.1 Cell Culture

Cell culture is the removal of cells from living tissue and their growth under controlled artificial conditions. [30] Two of the most commonly used prostate cancer cell lines are LNCaP and PC3. These are used to represent different behaviours of prostate cancer, with the LNCaP cells being more inactive than the PC3 cells, which are a highly aggressive form of prostate cancer. [31] The RWPE-1 cell line is the most common healthy prostate cell line.

In this thesis, the cell line that will be studied is the PC3. This cell line was derived from bone metastases of grade IV prostate cancer, from a 62-year-old caucasian male. [32] Additionally, for one assay, the RWPE-1 cell line will be used. This was derived from a 54-year-old caucasian male.

The most important difference between these two cell lines, in the scope of this thesis, is the fact that the tumourous cells have more GRP receptors in their membranes. This will cause the BBN-AuNPs to enter the tumour cells more easily and their concentration will be higher in these cells than in the healthy ones. Consequently, after irradiation, it is expected that there will be a higher radiosensitization effect in the tumour than in the healthy cells. [33]

3.2 Gold Nanoparticles

The AuNPs used in this thesis were coated with two different organic molecules, TDOA and TA-BBN resulting in AuNP-TDOA and BBN-AuNP-TDOA respectively. These organic molecules are represented in figure 3.1. These NPs were developed for theranostics research, which is why TDOA is used. It is a common molecule that can coordinate diagnostic and therapeutic radiometals, such as 67-Ga. BBN, as mentioned in section 2.5, is a peptide that will help the AuNP to more easily enter the cells, thereby

increasing its intracellular concentration.

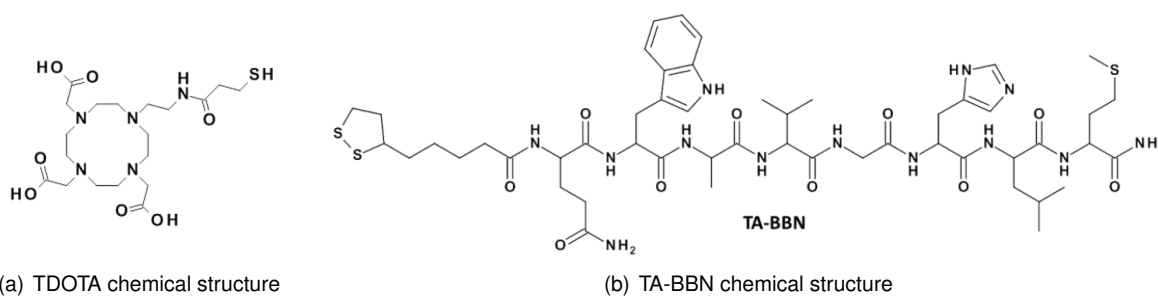


Figure 3.1: Chemical structure of the coatings used on the AuNPs for this thesis. Illustrations taken from [34].

Transmission electron microscopy (TEM) was used to obtain the core size of the AuNPs in a previous work [34], presented in figures 3.2 and 3.3. The AuNP-TDOTA had an estimated core size of (4.29 ± 1.60) nm and the BBN-AuNP-TDOTA of (4.79 ± 1.50) nm.

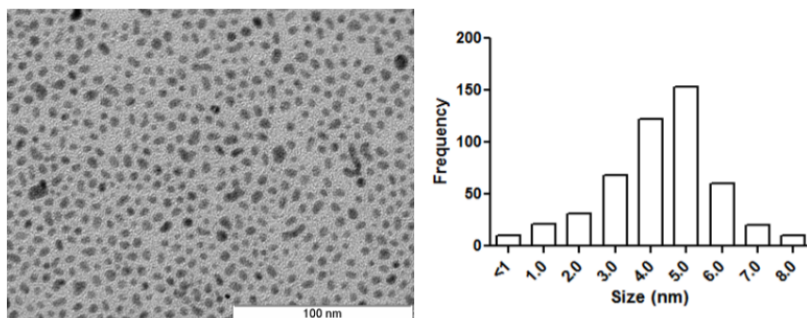


Figure 3.2: TEM image with respective size histogram of AuNP-TDOTA

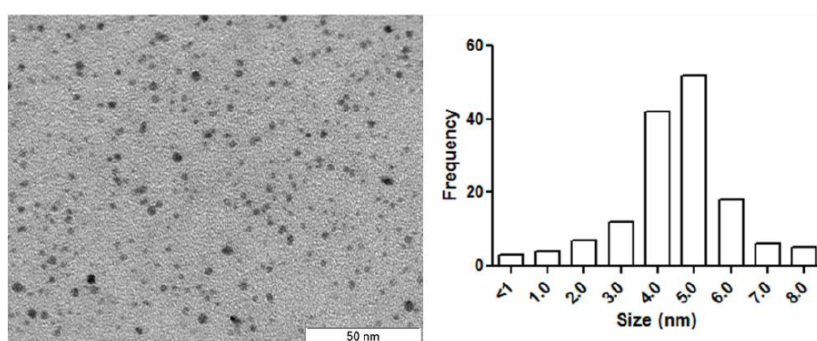


Figure 3.3: TEM image with respective size histogram of BBN-AuNP-TDOTA

For the irradiation studies a preliminary evaluation of the cytotoxic effect of both AuNP-TDOTA and BBN-AuNP-TDOTA was done. As can be observed from Figure 3.4, where several AuNPs concentrations (gold content) were used, there was no cytotoxic effect in the range 2-75 $\mu\text{g Au/mL}$. The concentration 36 $\mu\text{g Au/mL}$ was selected as a compromise to obtain a higher radiosensitizing effect with a negligible cytotoxic effect.

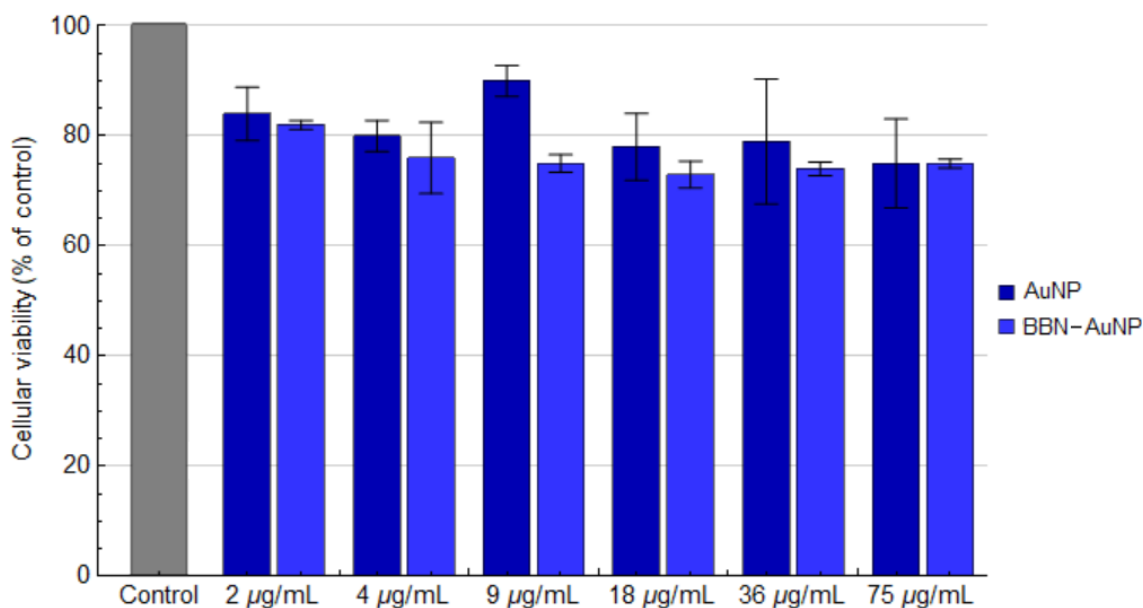


Figure 3.4: Selection of the AuNPs concentration for this study with the PC3 cells.

3.3 Irradiations

3.3.1 Precisa-22 Co-60 gamma rays

Some of the irradiations with Co-60 were performed in the Precisa-22 experimental irradiator (Graviner Manufacturing Company, Ltd) at CTN. It contains four sources placed inside stainless steel cylinders, where they move by the action of a pneumatic system. The sources are located in pairs on the two sides of the chamber where the samples are placed. These are mounted on a support that rotates automatically, in order to increase the dose rate uniformity. Two of these sources were in the irradiator originally and two were added later. In March 2020, it was estimated that the activity of the original sources was around 18 Ci each, while the activity of the recent sources was approximately 1 kCi each. The dose rate is determined by the position of the support inside the chamber, chosen as 1 Gy/min.

Ionization chamber

The dosimetric system used to obtain the average dose rate in the wells of the cell plates was the farmer ionization chamber FC65P.

This ionization chamber has air as the detecting medium. When a photon passes through the air inside the chamber, it creates electrons. The chamber then has two electrodes, with a voltage difference of 300 V between them: one is inside in contact with the gas and the other is the wall of the chamber. The electrons will move according to the electric field in the chamber, creating a current that can be measured with an electrometer. The number of electrons produced is proportional to the energy of the incident radiation. Therefore, this continuous current is proportional to the dose, depending on a calibration constant with units Gy/C for a specific type of radiation, under reference conditions of temperature, pressure and relative humidity.



Figure 3.5: Photo of the chamber of the Precisa-22 Co-60 irradiator.



Figure 3.6: Photo of the ionization chamber used to measure the dose rate. Taken from [35].

Dose rate uniformity

The dose rate varies for the different positions inside the chamber. Specifically, the dose rate will change for the different wells in the cell plate. Therefore, a first study was conducted for the 24- and 96-well plates in order to verify these fluctuations in the dose rate and choose the best wells to put our samples in. This was done with the ionization chamber and the support in figure 3.7.

The measurement was performed for only a few wells due to the circular symmetry of the setup, as we assumed that wells located at the same distance from the center of the plate would have the same dose rate applied to them. This study was conducted in two steps, described here.

STEP 1: The dose rate was measured three times in each well for 1 minute in order to establish a dose rate value of 1 Gy/minute. For this, we began the dose rate acquisition after the irradiation was started and calculated an average value of the dose rate.

STEP 2: To find the total incident dose on the cells in the real irradiation procedure, we took a few measurements where we began the irradiation after the data acquisition was started and only stopped this acquisition after the irradiation ended. Using this method, we performed irradiations during 30 and 60 seconds, in order to see if the total doses would be 0.5 and 1 Gy, respectively. This step was important to guarantee that even during shorter irradiations the total dose incident on the cells is precise

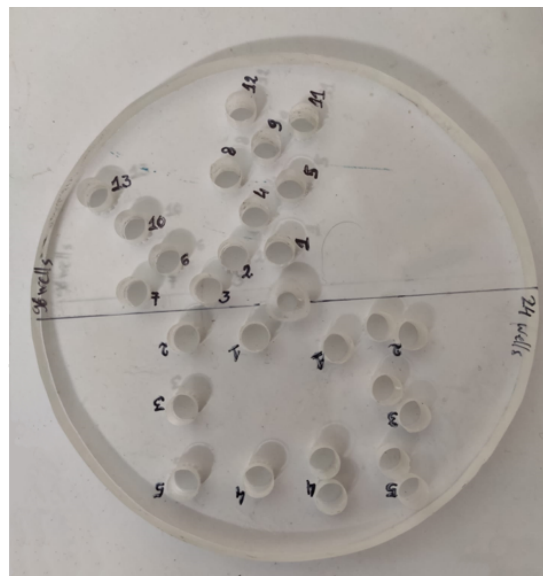
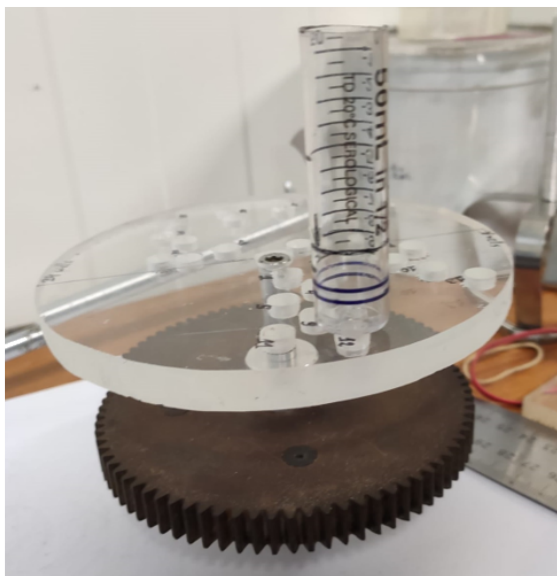


Figure 3.7: On the left, a photo of the setup that will be inserted in the Co-60 irradiator chamber, including a wheel to rotate the samples, an acrylic plate and a cylindrical support where the ionization chamber will be placed. On the right, the detail of the acrylic plate used to mimic the 24- and 96-well plates.

during all of the experiments, specifically taking into account the time it takes for the pneumatic system to bring the sources to the irradiation position.

3.3.2 Eldorado 6 Co-60 gamma rays

In order to see the impact of the dose rate on the radiosensitization effect of AuNPs, experiments were performed at a different Co-60 irradiator (Eldorado 6, by AECL Medical Products), with a much lower dose rate. This took place in the Metrology Laboratory of Ionising Radiation at CTN. The setup is in figure 3.8.

At a distance of 1 m, with this irradiator, the dose rate was 25.7 mGy/min. In order to achieve the 2 Gy, the cells were irradiated for 78 mins. The uniformity of the dose rate was guaranteed for the entire cell plate.

3.3.3 X-rays

Production of X-rays

X-rays originate from the conversion of electrons into photons after collisional or radiative interactions. These electrons are emitted from a heated filament (cathode) and subsequently accelerated by the application of a high voltage. The electrons will move towards the positively charged anode and interact with this target through several processes, described in section 2.3.2, the most relevant being bremsstrahlung emission. The output will be a continuous spectrum of X-ray energies with the maximum energy determined by the peak potential difference applied. Collimators are used in the end of the X-ray tube to better define the X-ray beam shape. [36] Filters can also be used, if necessary, to remove



Figure 3.8: Co-60 irradiation setup.

photons with unwanted energies from the beam.

Experimental setup

The irradiation with X-rays took place in the Metrology Laboratory of Ionising Radiation at CTN. The system contained a Philips MCN 165 X-ray tube and a YXLON 9421 high-voltage generator. The PTW IQ4-764 electrometer was used to measure air kerma. A photograph of the setup is in figure 3.9.

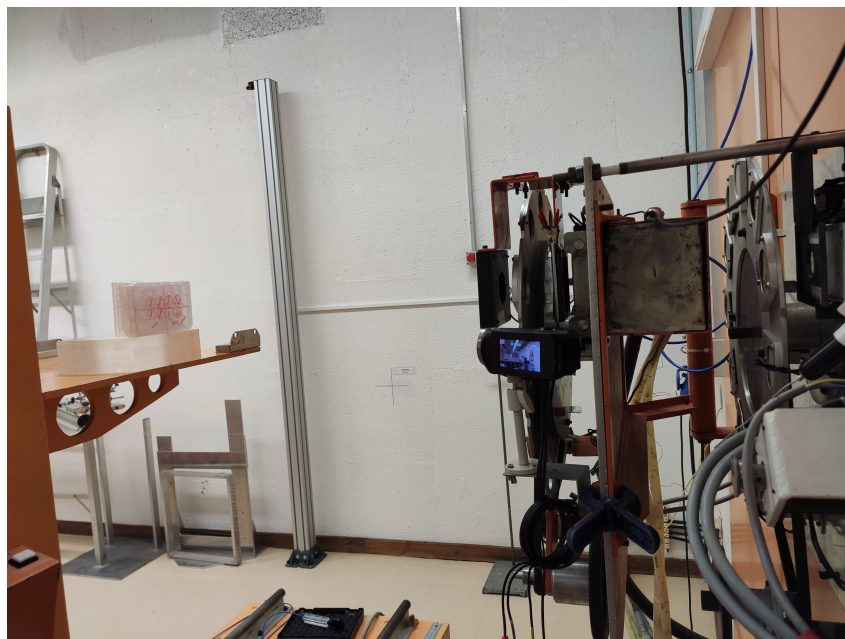


Figure 3.9: X-ray irradiation setup. The cell plate is visible on the left of the figure, aligned with the beam.

The ISO beam quality N100 was used, with a peak voltage of 100 kV and a mean energy of approx-

imately 84 keV, filtered with 4 mm Al and 5 mm Cu. This beam was chosen because this mean energy is just above the K-edge of gold and therefore, the Auger electron production from this shell is possible, increasing the dose enhancement effect of the AuNPs. The tube current was 20 mA and the distance from the cell plate to the source was 80 cm. The produced spectrum is in figure 3.10.

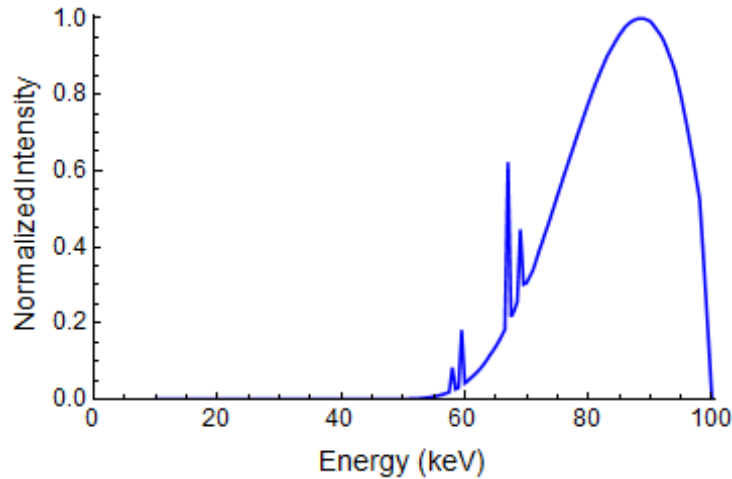


Figure 3.10: X-rays spectrum with the mentioned setup.

3.4 Clonogenic Assay

As mentioned in the section 2.2, a clonogenic cell is a cell that is able to reproduce and form a colony. Then, in a clonogenic assay, this reproductive ability of cells after irradiation is tested. This assay allows to obtain a plot with the surviving fraction of cells versus the dose they were irradiated with (survival curve). For more radiosensitive tissues, a small dose is enough to strongly decrease the surviving cells, while for tissues that are more radioresistant, a higher dose is required to obtain the same number of surviving cells.

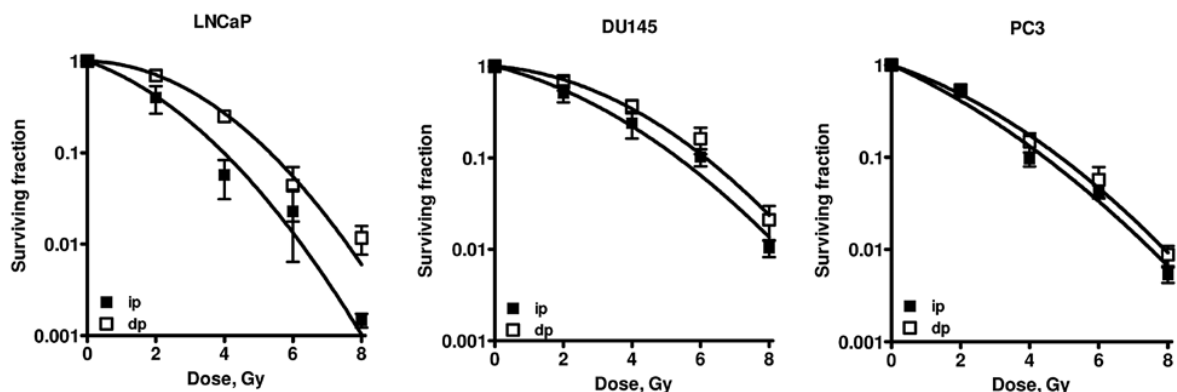


Figure 3.11: Example of the survival curves for 3 different prostate cancer cell lines, immediately plated (ip) or delayed plated (dp) 24h after X-ray irradiation. Adapted from [37].

Cells are seeded into a dish and incubated for a specific amount of time. During this time, each cell divides many times, forming a colony that is visible with the naked eye. The concept of plating efficiency

(PE) indicates the percentage of cells seeded that grow into colonies. Ideally, this would be 100%, however in reality there are uncertainties in the counting of the colonies, suboptimal growth media and mishandling of the cells.

$$PE = \frac{\text{Number of colonies counted}}{\text{Number of cells seeded}} \times 100 \quad (3.1)$$

Usually the surviving fraction (SF) is given by:

$$SF = \frac{\text{Colonies counted}}{\text{Cells seeded} \times (PE/100)} \quad (3.2)$$

The shape of the survival curve can be interpreted using the linear-quadratic model. This is a description that presumes that there are two components to cell killing by radiation, one proportional to the dose (D) and one proportional to the square of the dose (D^2). Therefore the expression for the cell survival curve is the following, in which α and β are constants:

$$SF = e^{-\alpha D - \beta D^2} \quad (3.3)$$

This is a good approximation of experimental results in the first decades of survival. [6]

3.4.1 Procedure for clonogenic assay

The cells were irradiated in 24-well plates, where each well contained a known number of cells. The cells were incubated with the NPs approximately 2 hours before the irradiation. Immediately after irradiation, they were transferred to 6-well plates, to make it easier to discriminate the colonies after they are formed. They were then left to grow for 13 days in the incubator.

After this time, the culture medium was removed from the wells and the cells were fixed with an ice-cold solution of methanol and acetic acid (3:1) for 20 minutes. Then the colonies were stained with a crystal violet solution for 7 minutes, rinsed with tap water and left to dry at room temperature. Subsequently the number of colonies was counted in all of the plates and the survival fraction for each dose was calculated. In this work, a collection of cells was considered a colony when there were more than 50 cells in the group.

3.5 Cytokinesis-blocked Micronucleus Assay

The cytokinesis-blocked micronucleus assay (CBMN) is widely used to measure DNA damage and cytotoxicity. In the scope of this thesis, it was performed to evaluate the effect of the presence of AuNPs in the cells and of the irradiation.

A micronucleus is a small body in the cytoplasm of cells that originated from damaged genetic material, such as chromosome fragments. In the CBMN, cytochalasin-B is used to block cytokinesis, the final stage of cell division, and the micronuclei are only scored in bi-nucleated cells, to prevent false results of micronuclei in non-dividing cells. [38]

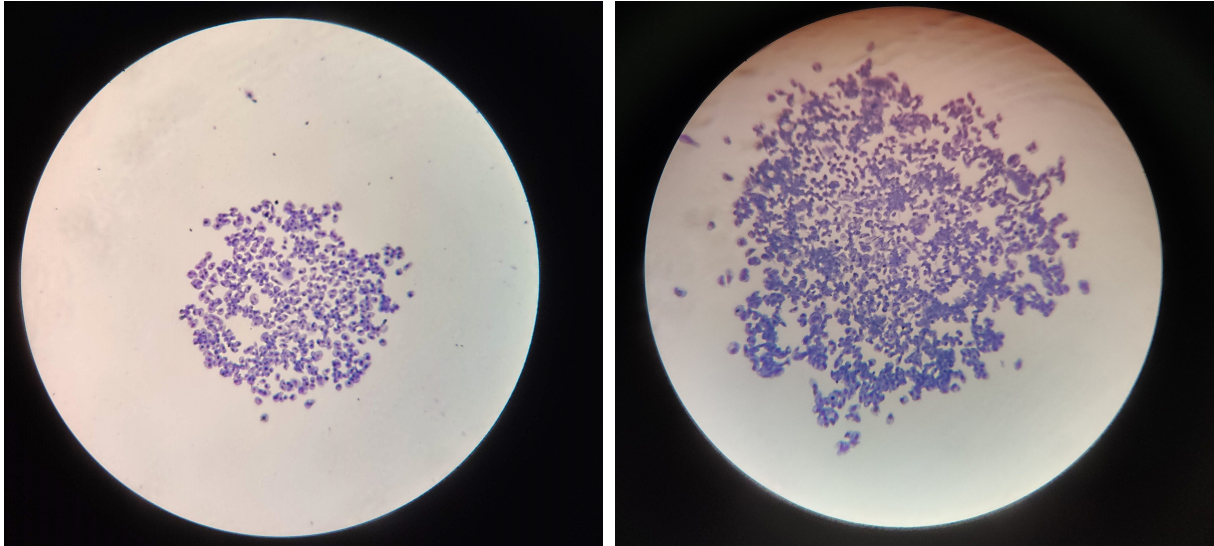


Figure 3.12: Examples of colonies from the clonogenic assay.

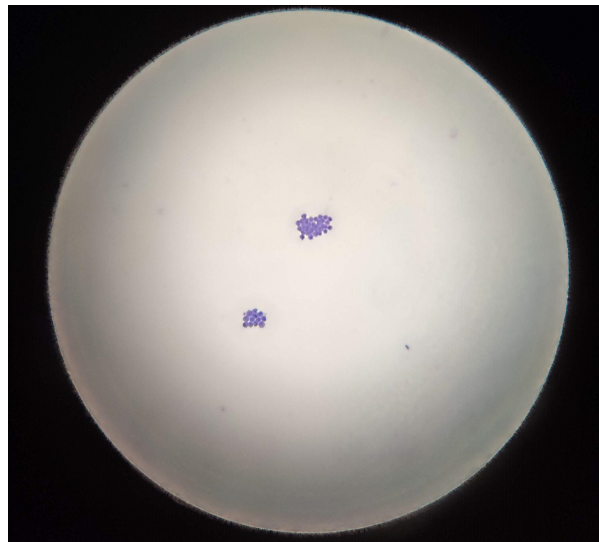


Figure 3.13: Example of groups of cells not considered colonies, because they contain less than 50 cells.

The criteria for scoring cells include mono-, bi- and multinucleated cells with one, two or more micronuclei with a diameter no greater than 1/3rd of the mean diameter of the main nuclei.

3.5.1 Procedure for the cytokinesis-blocked micronuclei assay

Following the irradiation, the cells were placed in the incubator for 22 hours. Then cytochalasin-B was added to each well at a concentration of 2 $\mu\text{g}/\text{mL}$, in order to inhibit cytokinesis, the final stage of cell division, and they were returned to the incubator.

After a total of 46h of incubation, the content of the wells for each dose was transferred to a 12 mL tube, carefully labeled. The tubes were then centrifuged for 10 minutes at 700 rpm at room temperature and a pellet of cells was formed at the bottom of each tube. The supernatant was removed, the tubes were agitated to loosen the pellet and the cells were washed with RPMI 1640 supplemented with

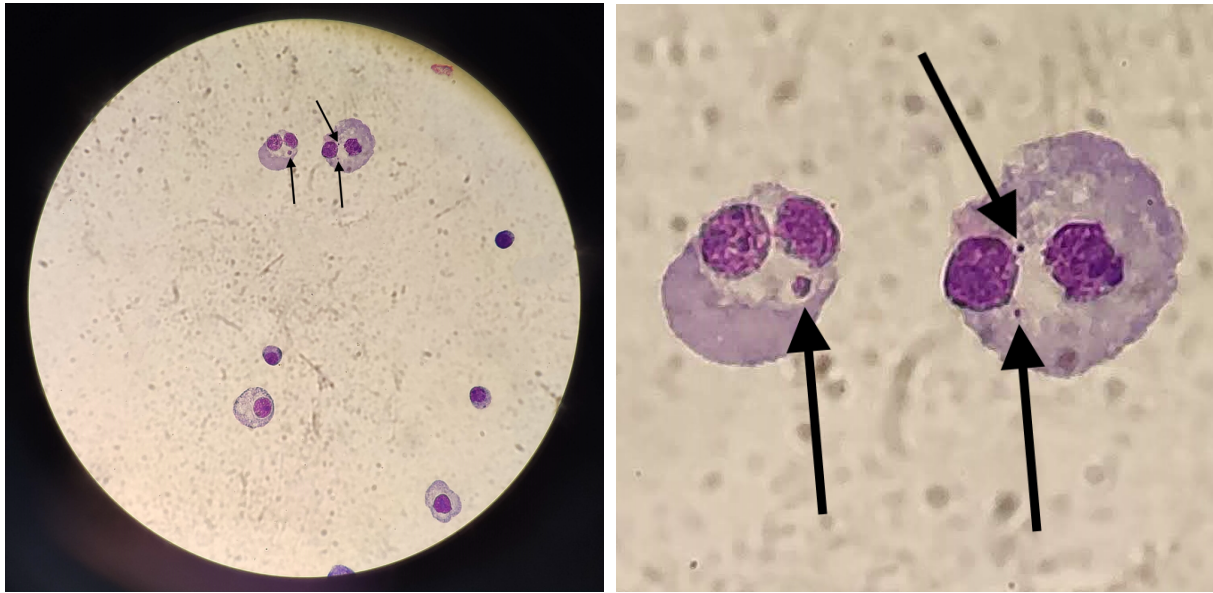


Figure 3.14: Photograph through a microscope of cells in the CBMN assay. Two cells are visible at the top of the figure in the left with micronuclei. The left cell has one and the right cells has two. The figure in the right is zoomed in on these cells.

FBS. The tubes were centrifuged again and the same procedure was repeated. Afterwards, the cells were subject to a mild hypotonic treatment, consisting of a mixture of RPMI 1640 and deionised water (1:4), supplemented with 2% FBS. The tubes were centrifuged one last time and the supernatant was removed.

Small drops of the remaining cell pellet were placed in clean dry slides, three for each dose, and the slides were left to air dry overnight. Subsequently the slides were fixed with ice-cold methanol/acetic acid (3:1) for 20 minutes and stained with a crystal violet solution for 7 minutes. They were rinsed with tap water, dried and closed with Entellan.

3.6 MTT assay

The MTT assay measures cellular metabolic activity to assess cell viability. It is based on the reduction of MTT (3-[4,5-dimethylthiazol-2-yl]-2,5-diphenyltetrazolium bromide), a yellow dye, to purple-colored formazan crystals, by enzymes on the mitochondria of living cells. The formazan is impermeable to the cell membranes, causing the crystals to accumulate in healthy cells. The absorbance of the product is analyzed with a spectrophotometer. The deeper the purple color (the higher the absorbance), the greater the concentration of formazan, indicating more viable cells in the well. [39] [40]

3.6.1 Procedure for the MTT assay

The PC3 cells (approximately 10000 cells/200 μ L) were seeded and allowed to adhere for 24 h. Then, a suspension of AuNPs with a concentration of 37 μ g Au/mL was added to the cells and incubated for 2 h at 37°C. After irradiation, the medium was discarded and the cells were maintained with fresh medium

for 72 h. Afterwards the medium was removed and 200 μL of a MTT solution in PBS (0.5 mg/mL) was added to the cells and incubated for 3 h. The formazan crystals formed by the reduction of MTT were dissolved in DMSO. The absorbance was measured at 570 nm with a Elisa reader.

The figure 3.15 is a photograph of a 96-well-plate after Co-60 irradiation and after DMSO was added to the cells. It is possible to observe that in the first column, containing untreated PC3 cells, the medium in the wells is darker than the rest of the columns. The third column (cells incubated with BBN-AuNP-TDOTA) contains the lighter purple colour and, therefore, the lowest concentration of healthy cells.

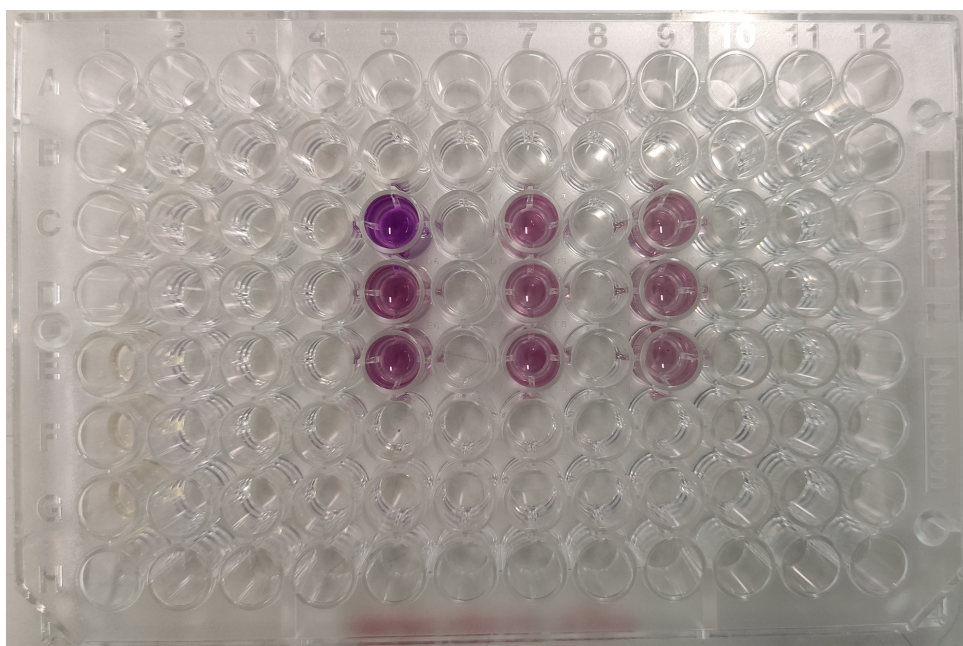


Figure 3.15: Photograph of an irradiated 96-well plate from the MTT assay. The first column with cells corresponds to untreated PC3 cells (control), the second column to PC3 cells incubated with AuNP-TDOTA and finally the third column to PC3 cells with BBN-AuNP-TDOTA.

3.7 Summary of the performed experiments

In the scope of this thesis, as mentioned before, three different irradiators were used: two of Co-60 gamma rays and one of X-rays.

For the procedures without nanoparticles, only the Precisa-22 irradiator was used. Two independent experiments were performed to obtain the survival curve of PC3 cells, at a dose rate of 1 Gy/min. In the first one, the total doses incident on the cells were 0.5, 1, 2 and 6 Gy and in the second one, a dose point of 4 Gy was added to the previous ones. For each of these doses, the cytokinesis-blocked micronuclei assay was also performed.

For the experiments with nanoparticles, the three radiation sources were used. The doses and dose rates for each are summarized in the table 3.1.

For all irradiations, clonogenic, micronucleus and MTT assays were performed. It was not possible to obtain a survival curve for PC3 cells with nanoparticles due to time and gold availability constraints.

Sources	Precisa-22	Eldorado 6	X-rays
Total dose (Gy)	2	2	74×10^{-3}
Dose rate (Gy/min)	1	25.7×10^{-3}	1.23×10^{-3}

Table 3.1: Radiation sources and respective dose points and dose rates.

Therefore a dose point was chosen, specifically 2 Gy, and the experiments with nanoparticles were performed at that dose for Co-60.

With X-rays, the total dose was very low compared to the ideal 2 Gy, because of two issues. First of all, there was a significant danger of overheating and damaging the X-ray tube if a higher tube current was used, which in turn restricts the dose rate. This would not be a problem if increasing the irradiation time was an option. However, as visible in figure 3.9, the plates were in a vertical position, which means that most of the cells are not in contact with a culture medium during irradiation and after some time without medium, the cells begin to die. This limits the irradiation time to about 1 h. Decreasing the distance from the plate to the source would also be an alternative, however the distance of 80 cm was the minimum distance that guaranteed the irradiation of the entire plate due to the divergence of the beam.

Additionally, a MTT assay was performed for the RWPE-1 cell line at Precisa-22, with the same dose and dose rate as for the PC3 cells, i.e. 2 Gy and 1 Gy/min.

In figure 3.16, there is a schematic representation of the NPs used, the cells and the irradiations. An important detail is the higher number of BBN receptors in the membrane of the cancer cell as opposed to the normal cells. This will cause a higher uptake of the NPs into the cells and decrease its radiosensitization effect in healthy tissues.

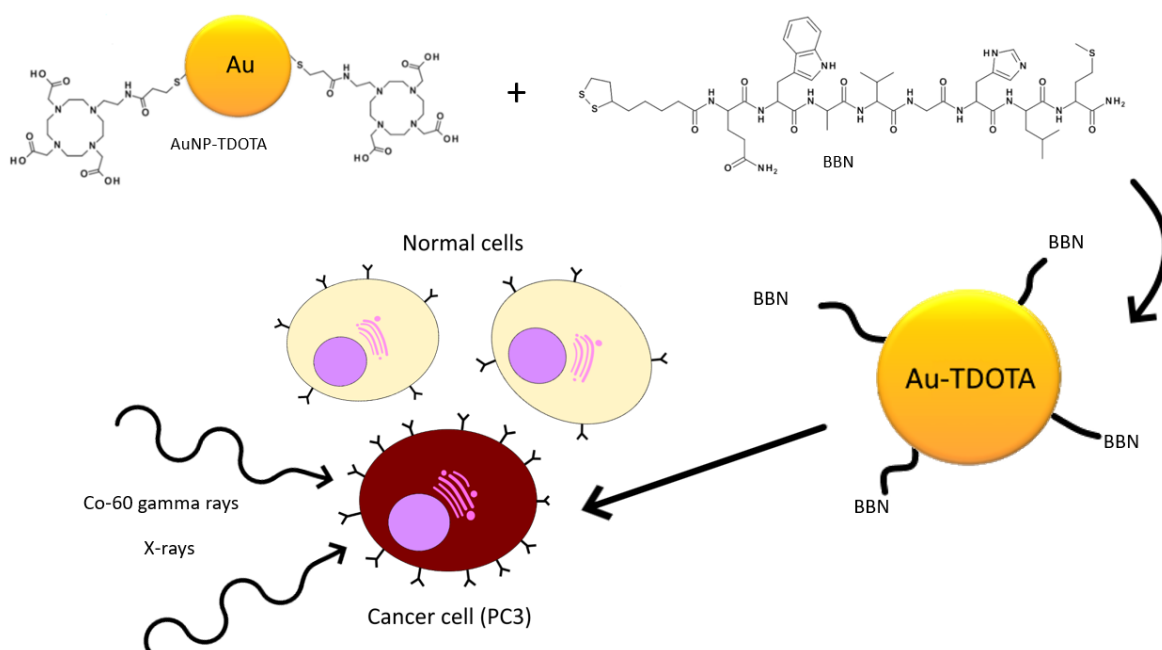


Figure 3.16: Scheme of the basic principles of the experimental procedures, including the NPs used and their ligands.

Chapter 4

Monte Carlo Simulations

In this chapter, there is a general overview of Monte Carlo simulation. An explanation of the simulations performed with PENELOPE and PenEasy is presented, including the geometry and spectra used.

4.1 PENELOPE

Monte Carlo simulations are a class of numerical methods based on the use of random numbers, that can solve complex physical and mathematical problems. In radiation physics, Monte Carlo methods are used to simulate the interactions between a beam of particles and the medium it traverses. The track of a particle is characterized by random variables, such as the distance between successive interactions, the type of interactions or the energy loss in the event, which are then applied to Probability Distribution Functions (PDF). Due to its nature, the results obtained by Monte Carlo methods have statistical uncertainties that can, however, be reduced by increasing the computation time.

PENELOPE is a Monte Carlo simulation code that describes the transport of photons, electrons and positrons in complex geometries, allowing the use of materials with arbitrary compositions. Its source code is written in Fortran-90 and it is constantly updated in the OECD Nuclear Energy Agency webpage. The version used for this thesis was PENELOPE2018. PENELOPE uses a mixed simulation approach, in contrast to the condensed history simulations of many softwares, which makes it ideal for detailed low-energy particle transport. It combines the detailed simulation of hard events (i.e., events with high polar angular deflection or high energy loss) with condensed simulation of soft events, that do not have a high impact on the particle's track. [41].

4.1.1 User-defined files

For the program to run, there are several files necessary, with all the simulation parameters defined. These files are described in the following paragraphs.

The **geometry file** (*.geo) is a text file describing the bodies in the simulation. PENELOPE allows for the use of complex geometries limited by quadric surfaces. The expression that defines a quadric surface is the following:

$$F(r) = I_1 \left(\frac{x}{\alpha_x} \right)^2 + I_2 \left(\frac{y}{\alpha_y} \right)^2 + I_3 \left(\frac{z}{\alpha_z} \right)^2 + I_4 \left(\frac{z}{\alpha_z} \right) + I_5 = 0 \quad (4.1)$$

A generic quadric surface is then fully defined by giving the set of indices (I_1, I_2, I_3, I_4, I_5), the scale factors that affect the axes ($\alpha_x, \alpha_y, \alpha_z$), Euler angles that define a rotation (OMEGA, THETA, PHI) and a displacement vector for translated surfaces (X-SHIFT, Y-SHIFT, Z-SHIFT). This geometry file contains these parameters for each surface, for all the bodies necessary to the simulation.

The **material files** (*.mat) are generated by the auxiliary program *material*. This is a program that extracts informations about a certain element or compound present in its database and compiles it in a text file. It is also possible to create a material that is not available in the database, by inserting its chemical composition and mass density, among other specific parameters.

PENELOPE must be complemented with a main program, which controls the geometry, records the relevant quantities, and performs the required averages at the end of the simulation. This main program is called by an input file. The **input file** (*.in) contains the simulation details, such as the source definition, the transport parameters and the wanted plots/results. There are different programs that can be used. They all contain this information, but some are more generic, while others are very straightforward and fast to use for specific purposes (for example, if the simulation presents cylindrical symmetry, the best program to use would be *pencyl*, which comes with PENELOPE). For this thesis in particular, the program used was PenEasy. [41]

4.1.2 PenEasy

PenEasy is a general-purpose main program for PENELOPE, that has specific tallies for the energy deposition in each material. The input file for the PenEasy program is divided into several sections.

- **Configuration:** this section contains the number of histories to simulate and the update interval of the output files. Additionally, it is possible to collect the results of the simulation in a dump file. This will allow the simulation to continue from where it previously stopped.
- **Source:** this is where the source is defined, including the particle type, position, direction and energy, whether it is monoenergetic or a spectrum.
- **Geometry:** this is where the name of the geometry file (*.geo) is inserted.
- **Transport:** in this section, there is a list of all material files that are mentioned in the geometry file. For each material, it is possible to establish the cut-off energies for photons (EABS(ph)), electrons (EABS(e-)) and positrons (EABS(e+)), the parameters C1 and C2, related to elastic events, the cut-off energy loss for hard inelastic collision (WCC) and hard bremsstrahlung emission (WCR), and finally the maximum step length of electrons/positrons in the body (DSMAX).
- **Tallies:** there is a section for each tally that PenEasy can create. The user can define if each of them is ON or OFF, according to the wanted results.

The tallies that were used in this thesis were the Energy Deposition Tally and the Particle Current Spectrum Tally. The first tally reports the energy deposited in each material in eV/history and the respective uncertainty (as 2σ). The second tally outputs the energy spectrum of the particles entering a specific material, classified according to particle type, as well as the total number of each type of particle.

4.1.3 Interaction forcing

Interaction forcing is a variance-reduction technique that can be used in PENELOPE and PenEasy. It artificially increases the probability of an interaction to take place, in order to reduce the uncertainties of the results of the simulation. In practice, this is implemented by PENELOPE through a change in the mean free path of the interaction, i.e. the mean free path of the real process is replaced by a shorter one, which is equal to the real mean free path divided by a user-defined forcing factor F .

To keep the simulation unbiased, a different weight is given to the secondary particles produced in this interaction, specifically, their weight is divided by the same forcing factor F , as well as the weight of the deposited energy by such particles.

The use of this method in this thesis lead to an increase of the energy deposited in the micro- and nanometric structures in the simulations and lower uncertainties. However, this technique violates energy conservation and, therefore, the results need to be carefully examined in order to understand if this process is significantly altering the outcomes of the simulations.

Interaction forcing can be activated in the input file, in the respective section, by indicating the type of particles and interactions that will be affected and the forcing factor. In the scope of this thesis, interaction forcing was only activated for inner-shell ionizations by electrons, since this is a process with a low probability that, however, is crucial for the dose enhancement in tumour cells loaded with AuNPs. All of the simulations with nanometric bodies presented in this thesis have a forcing factor of 1.5, unless stated otherwise.

4.1.4 Secondary Particle Equilibrium

The main problem when simulating the interactions of radiation with a nanoparticle is the very small target size. In order to obtain good results in a reasonable amount of time, it is common to simulate pencil beams with a width comparable to that of the NP, leading to simulations without lateral secondary particle equilibrium that will bias the results. In these cases, the beam width is smaller than the range of the secondary electrons and there will be an overestimation of both the DEF and the spatial range of the radiosensitization effect.

For example, with larger beams, there will be secondary electrons produced outside of the tracking volume that can however deposit their energy inside this volume, increasing the energy deposited in the body with and without the NP. If this effect was accounted for, the DEF would decrease. Additionally, there would be more Compton and Rayleigh interactions outside of the volume of the simulation that would interact with the NP, causing more secondary electrons to be produced. This would lead to an increase of the DEF.

4.2 MATLAB

MATLAB is a software for data analysis and algorithm development, among others.[42]

In this thesis, it was used mostly to facilitate the writing of large PENELOPE .geo files. In some simulations, it was necessary to create a large number of concentric spherical shells surrounding the NP to obtain the variation of DEF with distance. It was therefore easier to create a small script in MATLAB to write it automatically and, if some parameter needed to change (like the NP size), there was no need to write it all again manually.

Additionally, a few simulations were performed with several NPs. MATLAB was used to randomly distribute a specified number of NPs in a sphere with a defined radius, using the *rand* built-in function. The coordinates of these NPs were then used to automatically create the .geo file to run the simulations with PENELOPE.

4.3 Simulations performed

In the first simulations, several parameters were varied and the results were analyzed. These parameters were the distance between the source and the NP, the beam width and the NP size. Different geometries were used for the different simulations, which are explained in the next sections.

4.3.1 Variation of the distance between the NP and the source

The setup for the first simulations included a single NP with a diameter of 100 nm at the center of the tracking volume and a larger concentric sphere with a fixed radius of 1 μm . The world of the simulation was a cube with a length of 2 mm centered at the NP, which was adapted from Leung et al. (2011) [43]. This geometry is represented in figure 4.1. The source was defined as a plane with a length of 110 nm, emitting a parallel beam. The cut-off energy for all particles was set at 50 eV and the maximum step length for electrons (DSMAX) was one tenth of the thickness of each material. For this validation, the effect of the distance between the source and the NP was studied, for both Co-60 and X-rays. A value of the DEF was calculated for 4 distances: 10^{-4} cm, 10^{-2} cm, 10^{-1} cm and 1 cm, in the sphere of radius 1 μm .

In these simulations, there were 3 materials defined, one for each body on the geometry. Each material file was obtained with the PENELOPE material database, through the *material.f* program. The cubic world and the 1 μm sphere are made of water with a density of $0.99821 \text{ g cm}^{-3}$. The NP in the middle is made of gold, with a density of 19.32 g cm^{-3} , and then the simulations are repeated for a NP made of water, in order to see the effect of the gold NP.

The spectra used for the simulations are in the following plots. For Co-60, the spectrum consisted on the emission of gamma rays at 1.17 and 1.33 MeV. For the calculation of the X-ray spectrum, the program SpekCalc [44] was used, with the following parameters:

- Peak energy: 50 keV

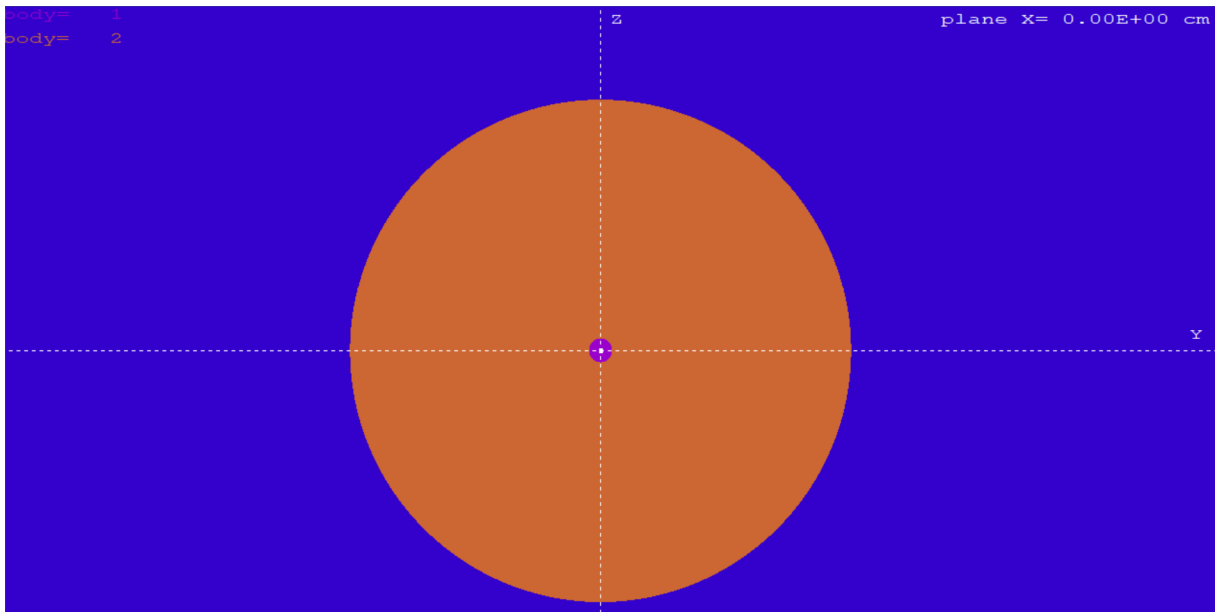


Figure 4.1: Representation of the geometry of the validation simulation, using the quadratic geometry viewing program *gview2d*, available in the PENELOPE package. The purple sphere in the center is the NP, the orange body around it is the $1 \mu\text{m}$ shell where the DEF will be calculated and the blue body around these spheres is the cubic world.

- Anode: Tungsten
- Anode angle: 20°
- Air thickness: 470 mm
- Beryllium thickness: 0.8 mm
- Aluminium thickness: 3.9 mm

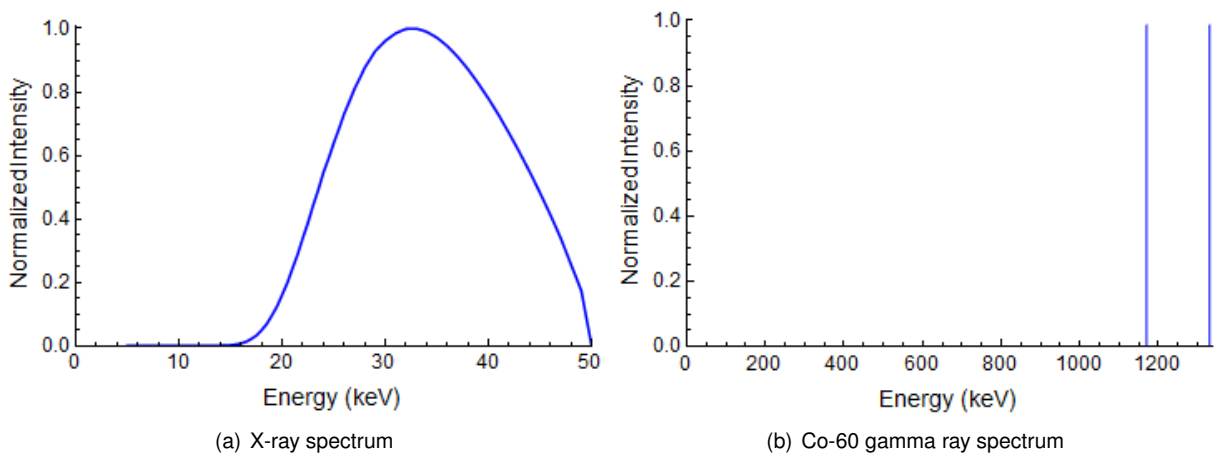


Figure 4.2: Spectra used in the validation simulations.

4.3.2 Variation of the NP size and beam width

The other parameters that were varied were the NP size as well as the beam width. Three different beam widths were chosen: for one of them (554 nm), nine NP sizes were simulated, and for the rest (654 and 800 nm), six NP sizes, making a total of 42 simulations. In this simulation, instead of the 1 μm shell, a simple cell model was used containing two concentric spheres to simulate the nucleus and the cytoplasm. Their dimensions were chosen to match an average PC3 cell, with the nucleus having a radius of 7.8 μm and the cytoplasm an outer radius of 11.3 μm . [45] In all of these simulations, the distance between the source and the NP was 50 μm .

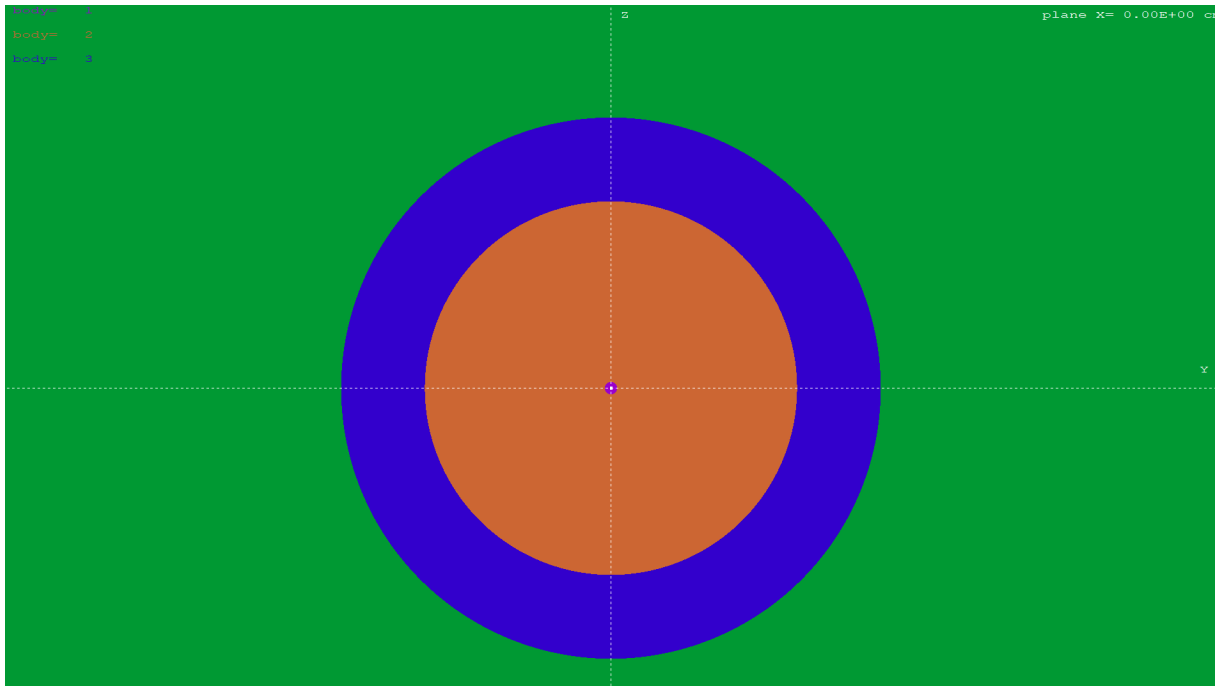


Figure 4.3: Representation of the geometry of the simulation where the NP size was varied, using *gview2d*. The purple sphere in the center is the NP, in this case with a diameter of 534 nm. The orange body around it is the nucleus and the blue body is the cytoplasm. The world of the simulation is the same as the previous one.

The biggest diameter was 534 nm and the rest were chosen as half of the volume as the previous one, giving approximately 440, 350, 277, 220, 175, 139, 110 and 87 nm. For the beams with 654 and 800 nm, the last three NP diameters were not simulated, because these simulations would not add any relevant information to the thesis.

4.4 Simulation with several NPs

Depending on the chosen concentration of gold in the cells, the number of NPs per cell can be around 10^5 or 10^6 . Simulating this amount of NPs will be not only time consuming but not allowed in PENELOPE, where the maximum number of bodies is 5000.

Therefore, instead of several small NPs, the simulations contained only one bigger NP and the effects were studied in the vicinity of this NP. Before running this simulation with the same concentration as the

experimental studies, a preliminary simulation was performed to verify that using one bigger NP or a lot of smaller NPs is, effectively, the same if the concentration of gold is the same. For this, simulations were made with a NP with a radius of 10 nm and 125 NPs with a radius of 2 nm each, corresponding to the same gold volume. They were performed for gold NPs and water NPs and the DEF was calculated in a water sphere with a radius of 100 nm. For the simulation with several NPs, they were randomly distributed in this 100 nm sphere and for the simulations with one NP, it was placed in the center of the sphere. The beam width was set to 200 nm and the distance from the source to the center of the NP was 1 μm . This was performed only for X-rays because it requires less computational time to achieve reasonable uncertainties. The spectrum was approximately the one in figure 3.10, the input parameters given to SpekCalc to calculate it are in section 4.5.

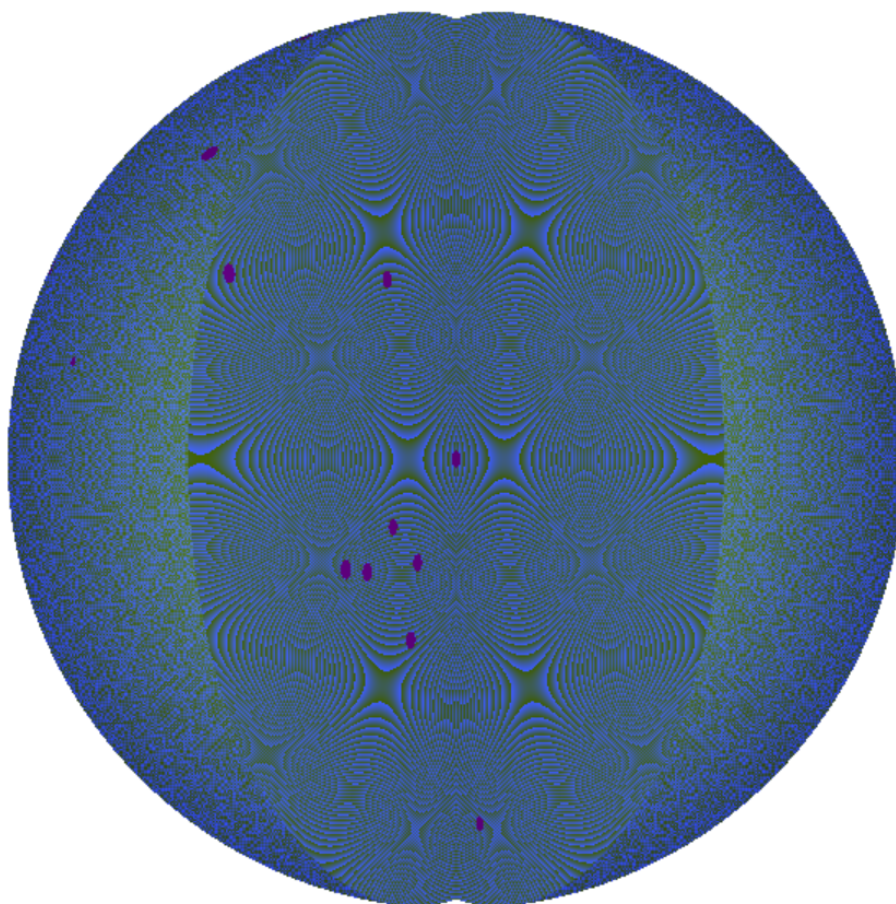


Figure 4.4: Geometry of the simulation with several NPs, using *gview3d*. The purple spheres are a few of the randomly distributed NPs and the bigger blue sphere is the 100 nm sphere where the DEF is calculated. In order to see the NPs, a wedge was created from -30 to 30° in the software.

4.5 Simulation of the experimental conditions

The AuNP concentration used for these simulations was 37.5 $\mu\text{g}/\text{mL}$. In order to decrease simulation time, instead of several small nanoparticles, the simulation contained only one bigger nanoparticle and

the effects were studied in the vicinity of this nanoparticle. The size of this nanoparticle was chosen so that the concentration of gold in the cell remained the same. The cell dimensions were the same as the simulations in section 4.3.2.

$$r_{NP} = \sqrt[3]{\frac{3}{4\pi V_{NP}}} \quad (4.2)$$

The volume of the gold core of the NP was calculated with gold's density ($\rho = 19.32 \text{ g cm}^{-3}$) and for the derivation of the mass, it was assumed that the gold corresponds to approximately 30.6% of the mass of the whole nanoparticle, a value taken from previous studies with these nanoparticles. Therefore,

$$m_{Au} = m_{NP} \times 0.306 \quad (4.3)$$

The mass of the whole nanoparticle was estimated considering the concentration of gold nanoparticles of $37.5 \text{ } \mu\text{g/mL}$ and the volume of a spherical cell with radius $10 \text{ } \mu\text{m}$.

$$m_{NP} = 37.5 \times 4.19 \times 10^{-9} \text{ } [\mu\text{g}] \quad (4.4)$$

Finally, the result obtained was a nanoparticle with a radius of 84.1 nm and consequently, this was the value used for all the simulations in the next sections.

The geometry used for the estimation of the DEF using the experimental conditions was approximately the same. Because this is a very localized effect, due to the very low range of the Auger electrons, instead of calculating the DEF in the whole cell, it was divided into shells. With PENELOPE, it was possible to determine the energy deposited into each shell, determine the respective dose and calculate the variation of the DEF with distance. The shells had a thickness of 100 nm .

Therefore, the geometry used was the one in figure 4.5. The DEF quickly decreased to 1 with distance and therefore, to decrease computational time, only the nucleus was simulated. In these simulations, the output was not only the energy deposited in each shell but also the type of particles deposited in the first and second shells closer to the NP.

These simulations, in general, were performed with several approximations, mostly to decrease computational time, and inherent PENELOPE limitations, namely:

- It was assumed that the cells have a spherical shape, with a nucleus that is centered in the middle of the cytoplasm. This is commonly assumed and it is acceptable for most simulations, but the influence of the shape of the cell in the radiosensitization of AuNPs is unknown.
- Only one larger NP was simulated instead of several smaller ones, as in the experimental procedures. The concentration of gold in the cell is the same, but because this is a very local effect, having one big NP or lots of small ones will cause different damages in the cells.
- The NP was placed in the nucleus, but in reality they are spread through the entire cell, including the cytoplasm.

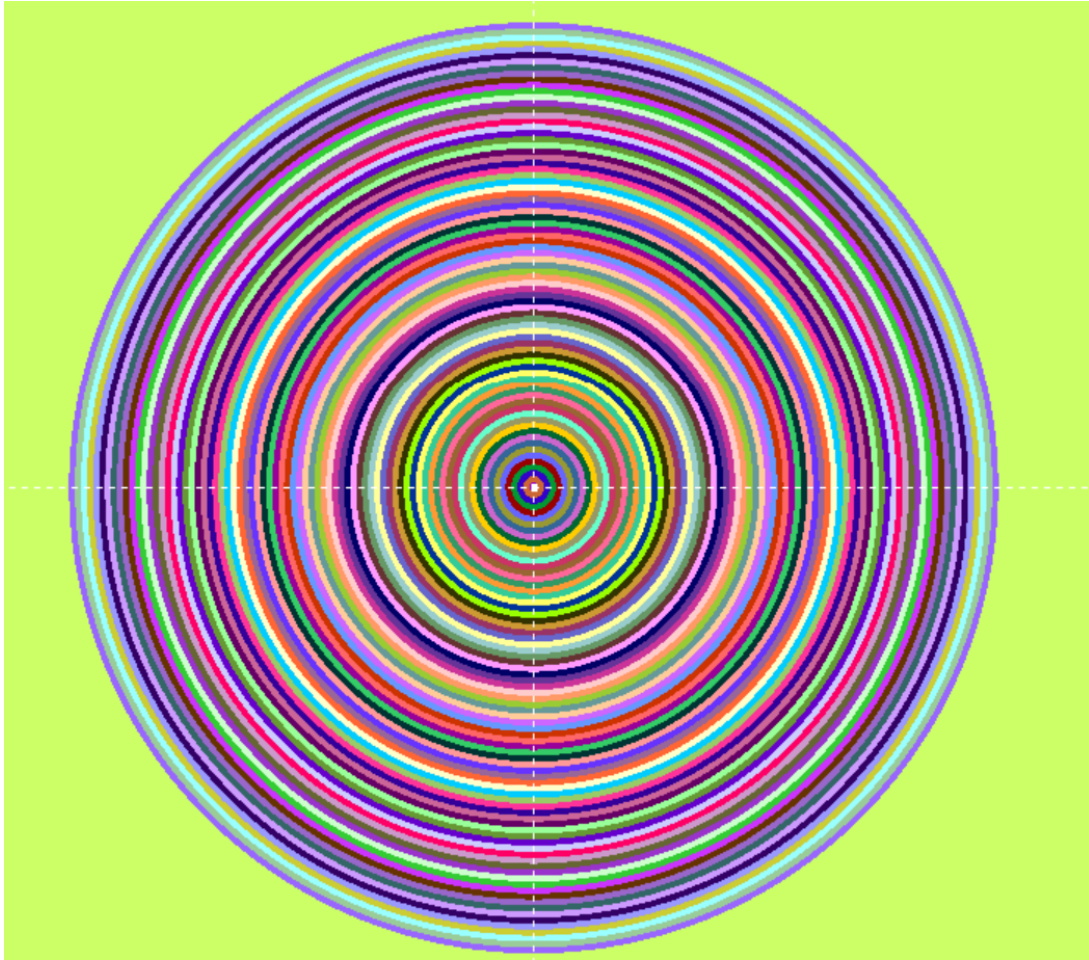


Figure 4.5: Representation of the geometry of the simulations with the experimental conditions, using *gview2d*. There were 78 shells, covering the nucleus of a PC3 cell with a radius of $7.8 \mu\text{m}$.

- The beams used in the simulations were smaller and secondary electron equilibrium is not guaranteed for some simulations.
- PENELOPE can only simulate the interactions with the materials for photons/electrons with an energy above 50 eV. This is a limitation specifically for nanometric simulations.

4.5.1 Co-60 irradiation

The spectrum used for the Co-60 irradiation was the same as before, in figure 4.2b. The distance between the source and the NP was estimated from the Precisa-22 irradiator, where the distance from the midpoint between the cylindrical sources on one side to the centre of the cell plate ($x;y;z$) is (127;102;146.5) mm. In the simulation, the distance used was the diagonal of the cube formed with the three previously mentioned distances, i.e. 21.91 cm. To reduce the computational time, a few approximations were taken: a planar source was simulated instead of an isotropic one and the beam width was reduced to 1 and $5 \mu\text{m}$.

4.5.2 X-rays irradiation

The spectrum used for the X-rays simulation was approximately the same as in the experiments, namely, the one in figure 3.10. This spectrum was obtained assuming a thickness of air of 80 cm after the source and therefore, this distance was not added to PENELOPE. The distance between the source and the cell was then only 12 μm , a value just above the 11.3 μm corresponding to the cell radius. The characteristics of the spectrum, given as input to the SpekCalc software were:

- Peak energy: 100 keV
- Anode: Tungsten
- Anode angle: 22°
- Air thickness: 800 mm
- Aluminium thickness: 4 mm
- Copper thickness: 5 mm

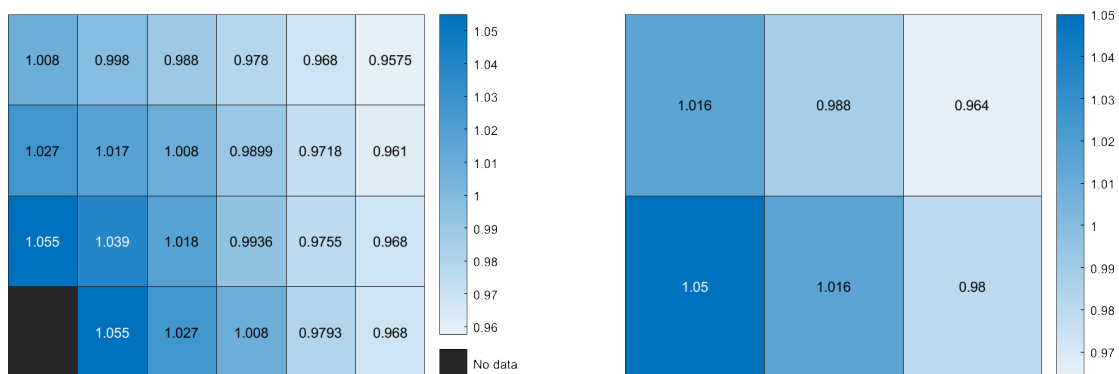
The beam width was the minimum value possible that could provide secondary particle equilibrium, i.e. 50 μm for the NP with a radius of 84.1 μm and the cell with the radius of 11.6 μm . The world was again cubic with an edge of 25 cm.

Chapter 5

Results

5.1 Dose rate uniformity with Precisa-22

The values of the dose rate in the wells of the 96- and 24-well plates are in figure 5.1. The measurements are shown in only one quarter of each plate because, as mentioned in section 3.3, wells at the same distance from the center have the same dose rate applied to them. There is no data in the 4 wells in the centre of the 96-well plate because it is where the acrylic plate was supported by a vertical axis (figure 3.7). The calculated uncertainties in all of the wells were below 5%.



(a) Dose rates in one quarter of a 96-well plate

(b) Dose rates in one quarter of a 24-well plate

Figure 5.1: Dose rates in the wells of one quarter of each cell culture plate. All values are in Gy/min.

The variations from the wanted value of 1 Gy/min were very small and the overall variation of the dose rate in the plates was below 10%. With these values, the layout of the cells in the plates was as described in image 5.2, where the wells in which the cells were placed were the ones where the dose rate was closest to 1 Gy/min and more uniform.

All of the procedures in this thesis for the irradiation with Precisa-22 followed this layout.

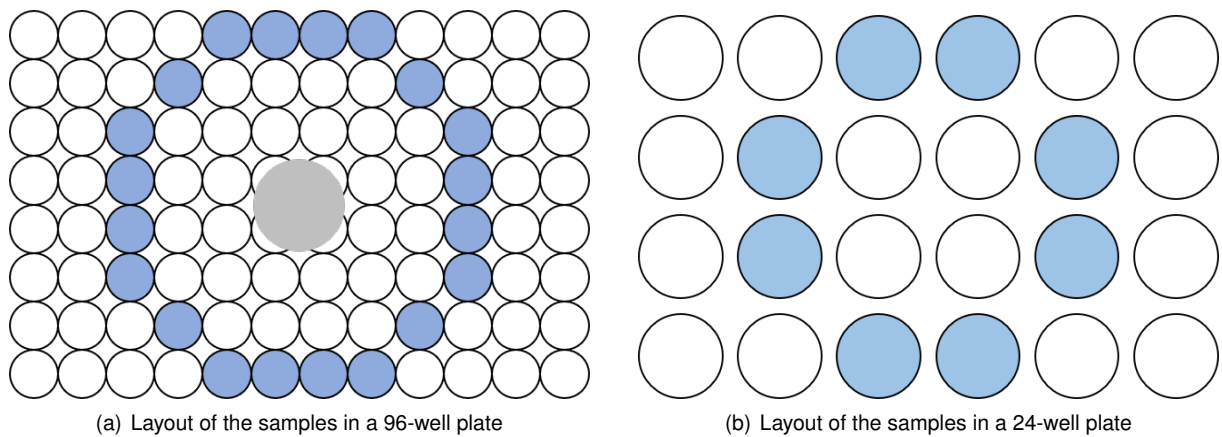


Figure 5.2: Layout of the samples in culture plates. The blue corresponds to the wells containing cells. The remaining wells were empty.

5.2 Experiments without gold nanoparticles

5.2.1 Clonogenic assay results

The clonogenic assay allowed for the estimation of the survival curve for PC3 cells in the Precisa-22 irradiator. The results are in figure 5.3. The data points are plotted as well as the equation obtained for the survival curve (equation 5.1). The residuals of each data point are also presented in figure 5.4.

$$SF = e^{-0.477 D - 0.007 D^2} \quad (5.1)$$

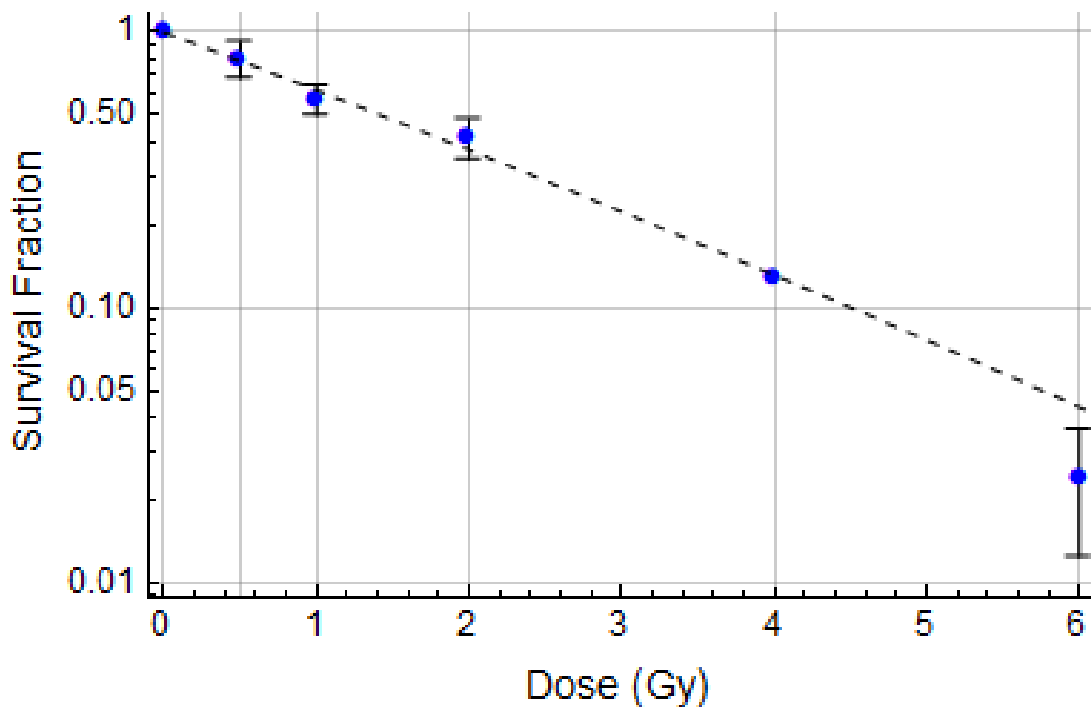


Figure 5.3: Survival curve of PC3 cells after irradiation with Co-60 gamma rays, at a dose rate of 1 Gy/min. The point of 4 Gy does not have an uncertainty, because only one assay was performed for this dose.

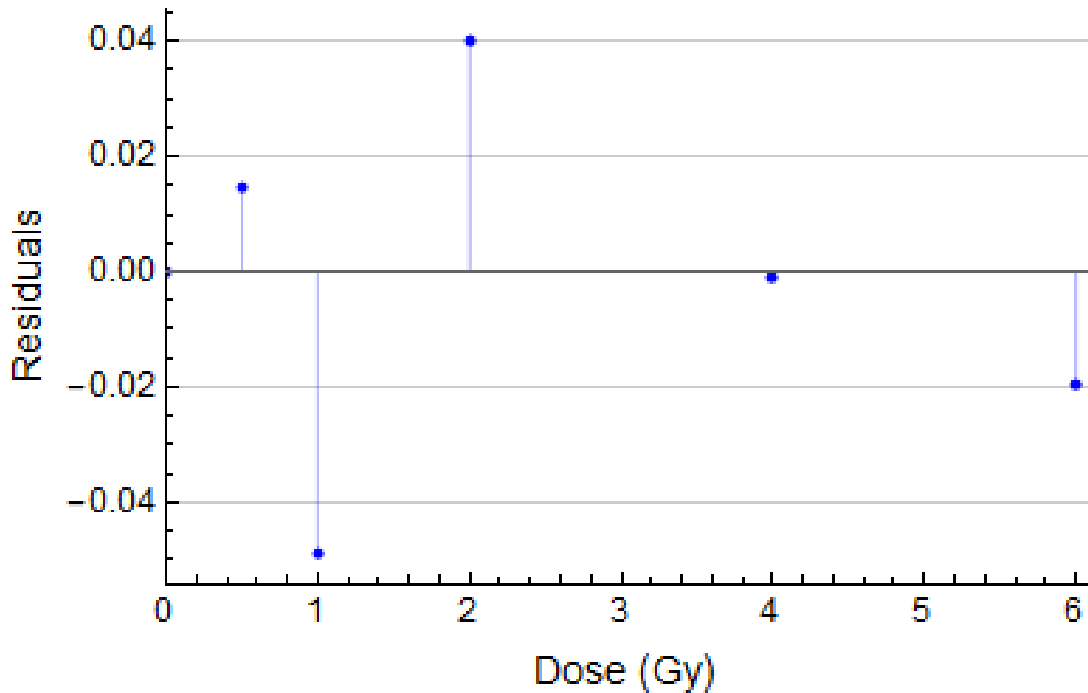


Figure 5.4: Plot of the residuals of each measurement relatively to the equation 5.1.

It can be seen that the survival curve follows the expected tendency, with the survival fraction decreasing with the increasing dose in the cells. The model used, as mentioned in section 3.5, was the linear-quadratic one. From both figures 5.3 and 5.4, a discussion about how well this model fits the data can be made. Looking at the survival curve alone, the model is within the uncertainty intervals of every point, with exception of the lowest survival fraction for 6 Gy (but, as stated in section 3.5, this model is only used for the first decades of survival). When looking at the residuals plot, the model seems to be a good fit. Ideally, if this was the case, the residuals would be random and there would be approximately the same number of positive residuals as negative ones. In this case, there is no obvious tendency in the residuals, however there are not enough data points to say this for certain. Nonetheless, with the available information, this model seems to be a good fit of the experimental points.

5.2.2 CBMN assay results

CBMN assays were also performed for the various dose points, to evaluate the damages in the DNA of the cells with the irradiation alone. The results are in figure 5.5. The micronuclei yield is the number of micronuclei counted divided by the total number of binucleated cells scored. In this particular case, two assays were performed in different days and the total number of scored cells was not the same for both assays. Therefore, instead of a regular arithmetic mean, the presented results are the weighted mean of the micronuclei yield of both assays.

It can be seen that, as expected, the number of damages increases with the dose in the cells. For the control cells, that were not irradiated, the micronuclei yield is 0.04 ± 0.02 and not zero, indicating that there were still some damages even without the irradiation. These can occur due to, for example, mishandling of the cells during the assay and culture. The micronuclei yield rises to 0.64 ± 0.07 when

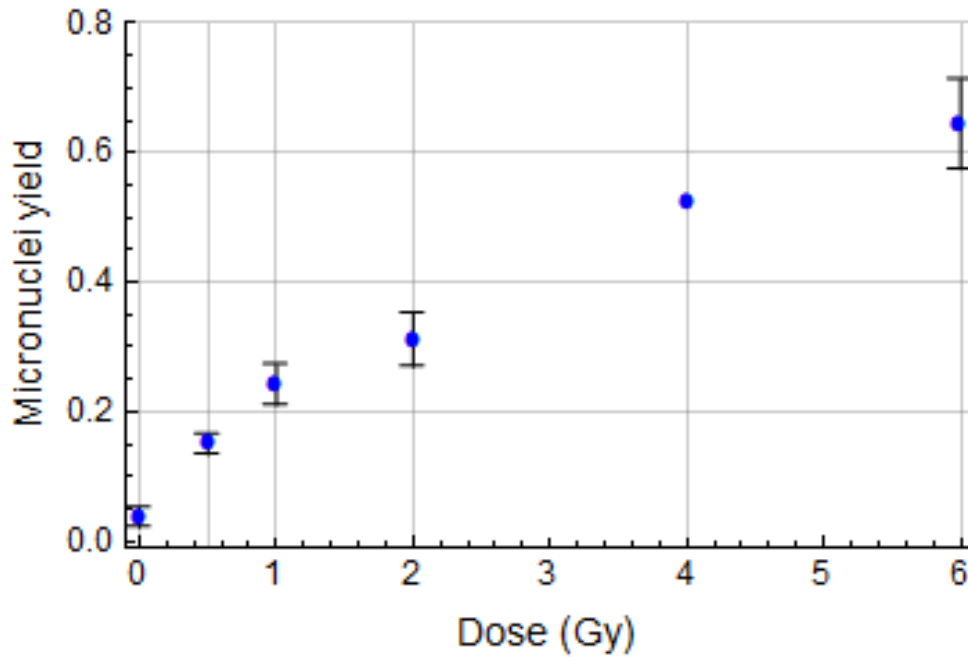


Figure 5.5: CBMN assay results for PC3 cells. Once again, only one assay was performed with a total dose of 4 Gy.

the cells were irradiated with a total dose of 6 Gy.

Based on the results of these assays, the total dose of 2 Gy was chosen for the studies with NPs. This was a dose point with an intermediate value of cell death, enough for the radiosensitisation to appear but not so high that almost all of the cells die and no conclusions can be drawn regarding the effect of the NPs. This dose is also common in radiotherapy treatments with dose fractionation.

5.3 Experiments with gold nanoparticles

5.3.1 CBMN assay results

The results of the experimental part are presented in chronological order. The CBMN assay gives results of the damages in the DNA of the cells after one cell division. The MTT assay allows for the estimation of the cellular viability after 3 days (roughly 3 cellular divisions), while the clonogenic assay evaluates the survival of the cells after 13 days. Comparing the differences between these assays can give an idea not only of the short-term effects of the irradiation and presence of NPs but also of how the cells repair the damages.

The results of the CBMN assay are in figure 5.6 for the three radiation sources. The results are calculated as the number of micronuclei divided by the number of scored binucleated cells (this ratio is called the micronuclei yield). These values are then normalized to each control, i.e. for example for the cells incubated with AuNPs, the plot contains the value of the micronuclei yield in the irradiated sample divided by the value of the micronuclei yield in the control cells incubated with AuNPs but not irradiated.

Several conclusions can be drawn from the plot in figure 5.6. First of all, the effect of the irradiation is

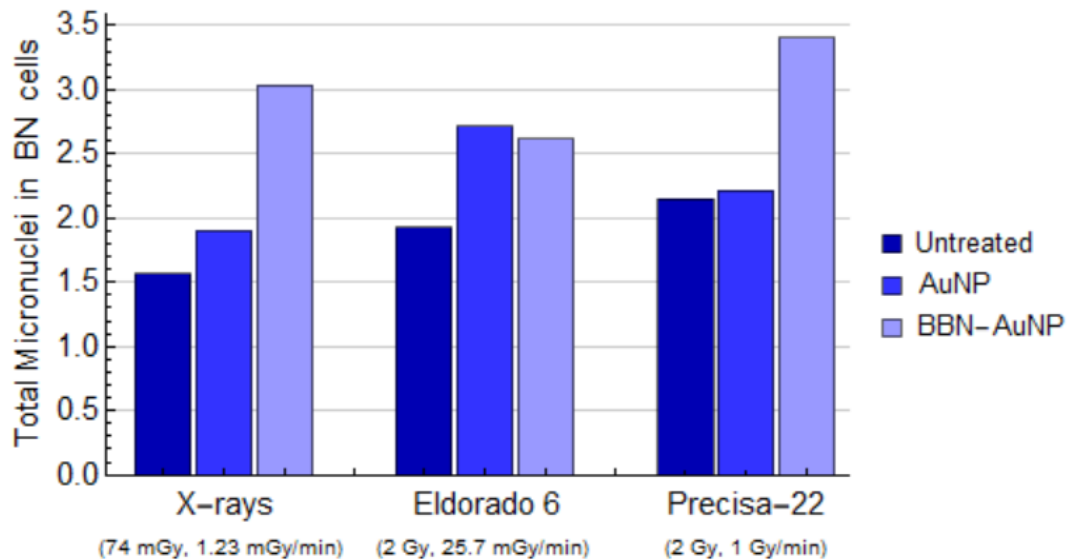


Figure 5.6: Micronuclei yield in binucleated (BN) cells, normalized to each control.

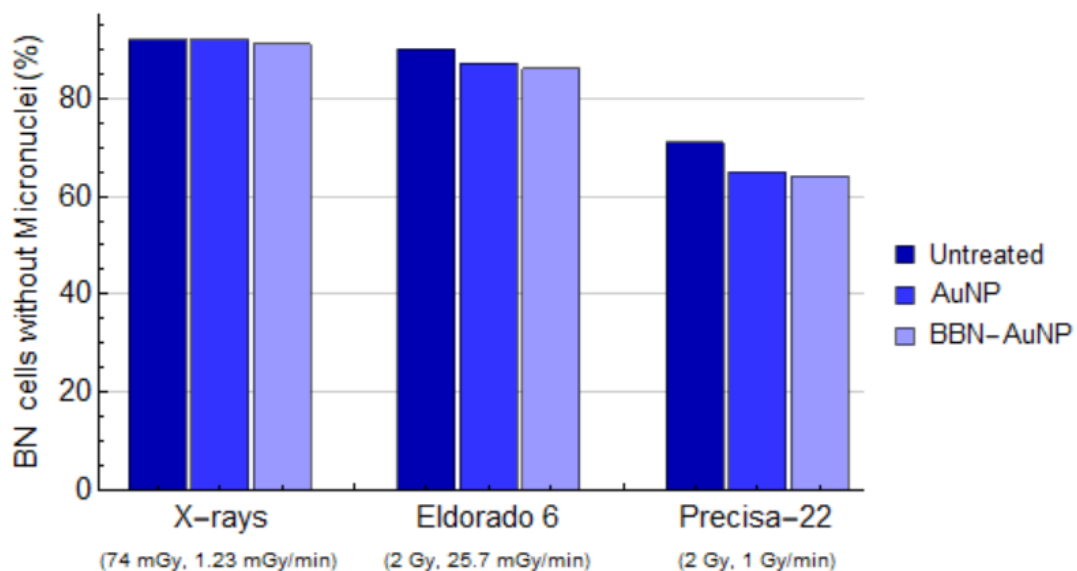


Figure 5.7: Binucleated cells without micronuclei, as a percentage of the scored cells.

evident. For Co-60 gamma rays, the micronuclei yield in the irradiated samples is approximately twice as high as the micronuclei yield in the control cells. For X-rays, the difference is smaller, the yield increases around 50% with the irradiation. The X-rays caused less damage because the total incident dose on the cells was lower.

Regarding the effect of the NPs, there is a clear difference between the irradiated cells with and without AuNPs for X-rays and Co-60 gamma rays in the Eldorado 6 irradiator. This difference is not significant in the Precisa-22 irradiator. However, when comparing the cells incubated with AuNPs and BBN-AuNPs, for X-rays and in Precisa-22, there is a clear increase in the DNA damages for the PC3 cells with BBN-AuNPs.

The radiosensitization effect of the NPs is proved in this assay. The samples incubated with BBN-

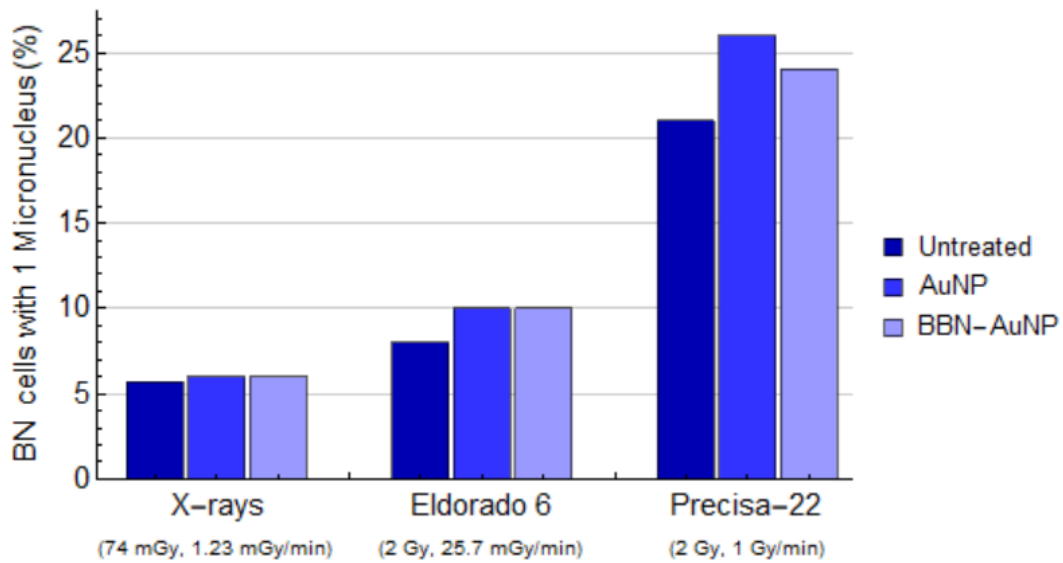


Figure 5.8: Binucleated cells with one micronucleus, as a percentage of the scored cells.

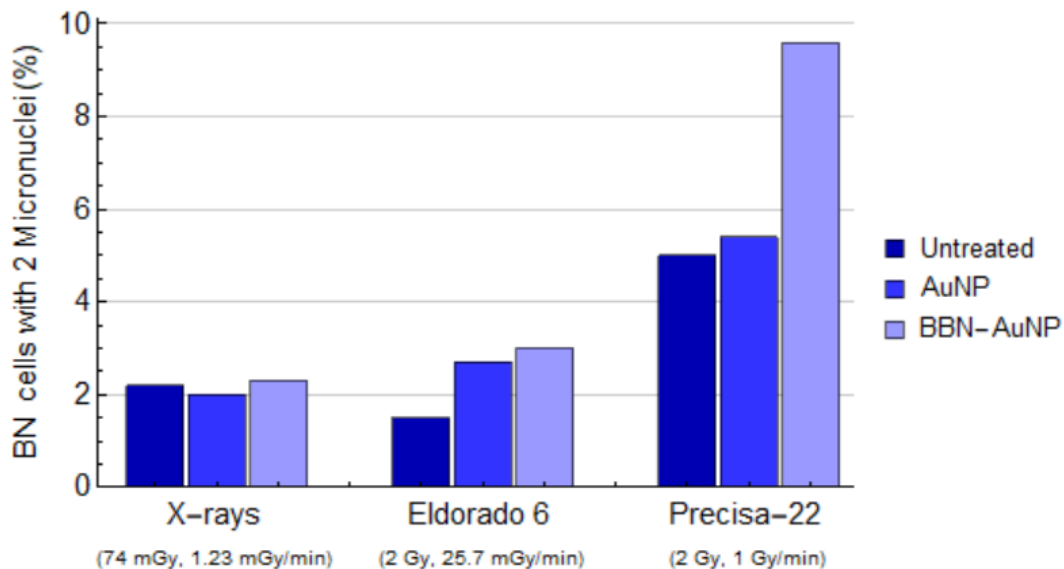


Figure 5.9: Binucleated cells with two micronuclei, as a percentage of the scored cells.

AuNP with all three sources show more micronuclei than the irradiated cells without any NP. Compared to the irradiated PC3 cells, with the Eldorado 6 irradiator, there is an increase of 40% of the micronuclei yield; with Precisa-22, the increase is of the order of 60% and with X-rays, there is a 93% increase. It is possible to conclude that, even though the total dose in the cells with the X-ray irradiation is lower, the effect of the addition of BBN-AuNPs is higher for this radiation, as expected from the differences in the mass attenuation coefficient of gold and water (figure 2.5).

Despite the fact that X-rays cause a higher radiosensitization effect of the AuNPs, the damages caused by this radiation are more easily repaired by the cell, as can be seen in figures 5.9 and 5.10. In these, the percentage of binucleated cells with 2 and 3 micronuclei is presented, respectively. For comparison purposes, the figures 5.7 and 5.8 contain the percentage of binucleated cells without micronuclei

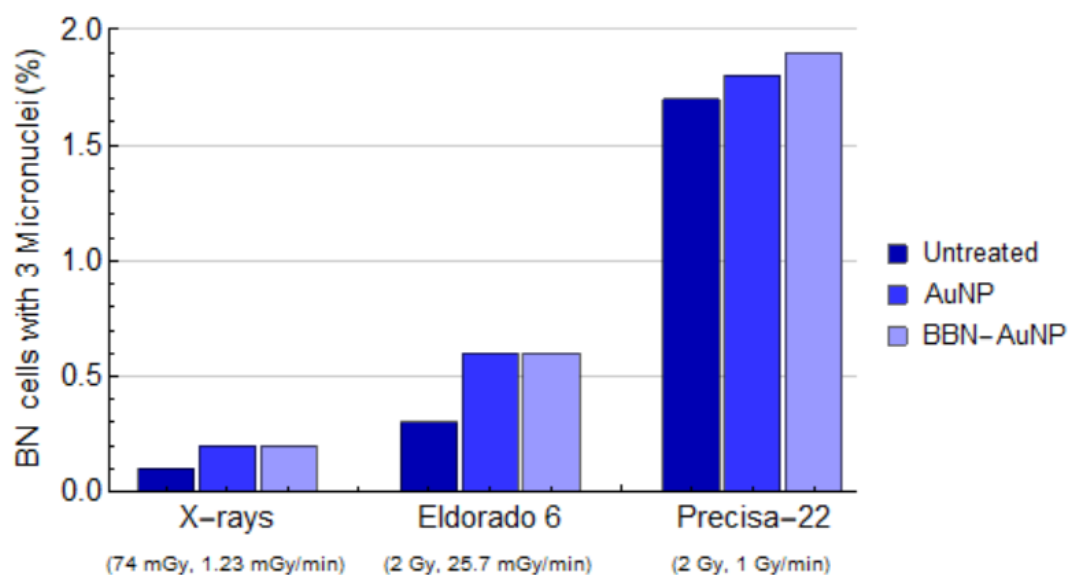


Figure 5.10: Binucleated cells with three micronuclei, as a percentage of the scored cells.

or with only one. It can be seen that the Co-60 gamma rays from Precisa-22, with the highest dose rate, is the radiation that causes a higher number of damages inside the cells. For PC3 cells only, around 7.5% of the binucleated cells have more than 1 micronuclei and this number increases to 11.5% when the cells were incubated with BBN-AuNPs. For X-rays, this value is around 2% and remains constant for cells with NPs. In all plots, there is a clear higher damage in the cells after the Precisa-22 irradiation, however the damages caused by the X-rays are similar to those caused by the Eldorado 6 irradiation even though the dose in the cells in the latter is much higher.

5.3.2 MTT assay results

The MTT assay allows for the estimation of the cellular viability three days after the irradiation, i.e. approximately after three cell cycles have occurred and some damages were repaired.

The results are in figure 5.11. They were calculated as the ratio between the cellular viability in the irradiated sample and the cellular viability in the respective control. For example, the results of the *BBN-AuNP* bars were calculated as the cellular viability for the irradiated cells incubated with BBN-AuNPs as a percentage of the cellular viability on the cells incubated with BBN-AuNPs that were not irradiated.

It is possible to conclude that after three days, there are no differences when comparing the three radiation sources. The cellular viability of the irradiated cells is the same in the three cases, when taking into account the uncertainties of the values. There is also no significantly higher radiosensitization effect of the BBN-AuNPs when compared to the AuNPs.

It can be seen however that there is a difference between the cells incubated with and without NPs. For X-rays and Co-60 gamma rays in the Eldorado 6 irradiator, there is a decrease of the cellular viability of around $(23 \pm 15)\%$ and $(27 \pm 5)\%$ respectively, when the irradiated cells were incubated with BBN-AuNPs. With the Precisa-22 irradiator, this decrease in the cellular viability was of the order of $(33 \pm 21)\%$.

Additionally, only for this assay, it was possible to perform the irradiation with RWPE-1 cells at

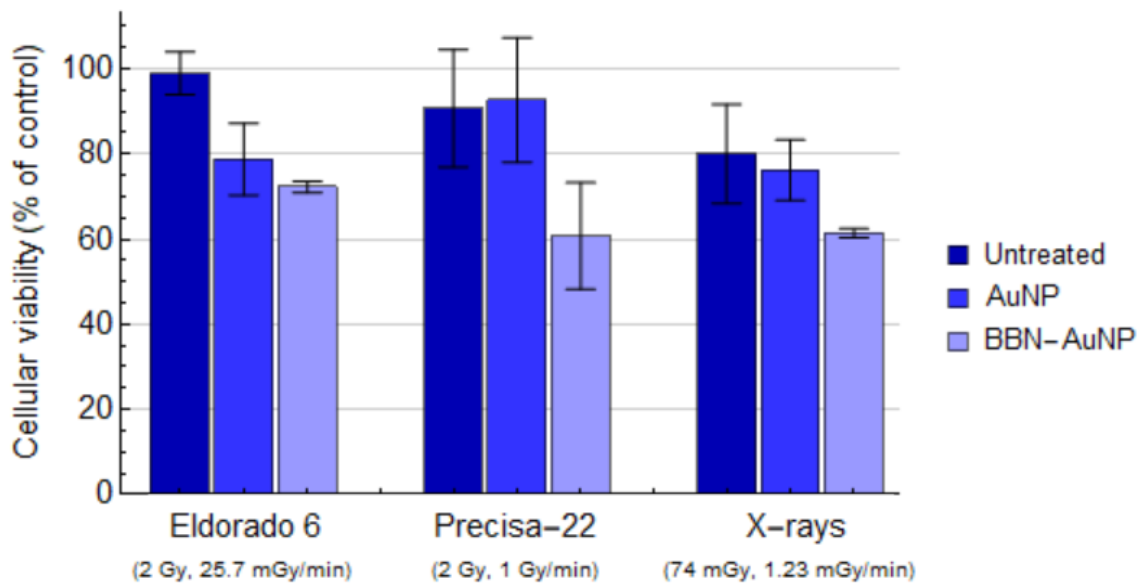


Figure 5.11: Cellular viability as a percentage of each control.

Precisa-22. Since tumorous cells have more receptors, the NPs will more easily enter the cells and cause more cell damage after irradiation. It is therefore expected that with the RWPE-1 cell line, there is a lower concentration of NPs inside the cells and the cellular viability of the samples should be higher than for the PC3 cell line. These results are in figure 5.12 and verify these assumptions, as the cellular viability as a percentage of each control remains constant and there is no damage after irradiation.

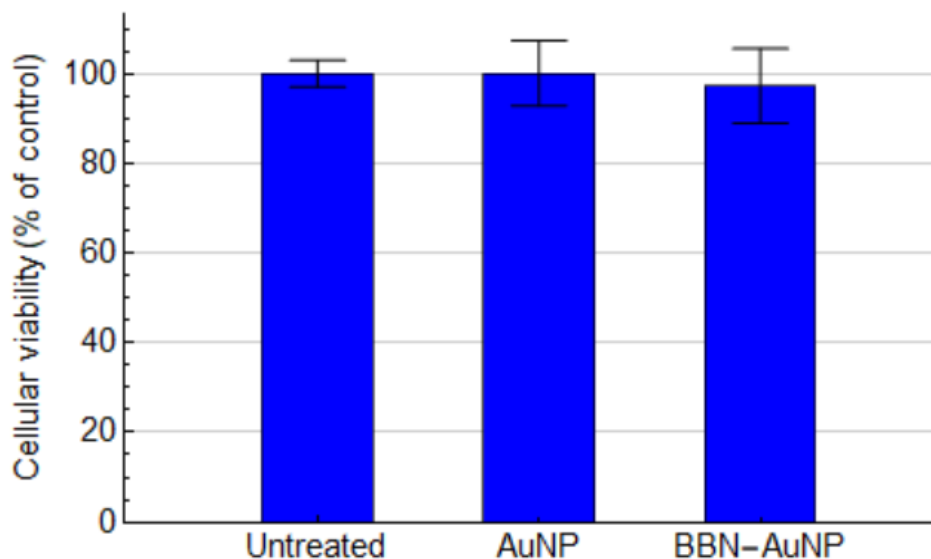


Figure 5.12: Cellular viability as a percentage of each control, for the RWPE-1 cell line.

5.3.3 Clonogenic assay results

The clonogenic assay allows for the evaluation of the survival cells after a longer period of time, specifically in this thesis 13 days.

The results are in figure 5.13. They were all calculated as a percentage of the respective control, similarly to the MTT assay results.

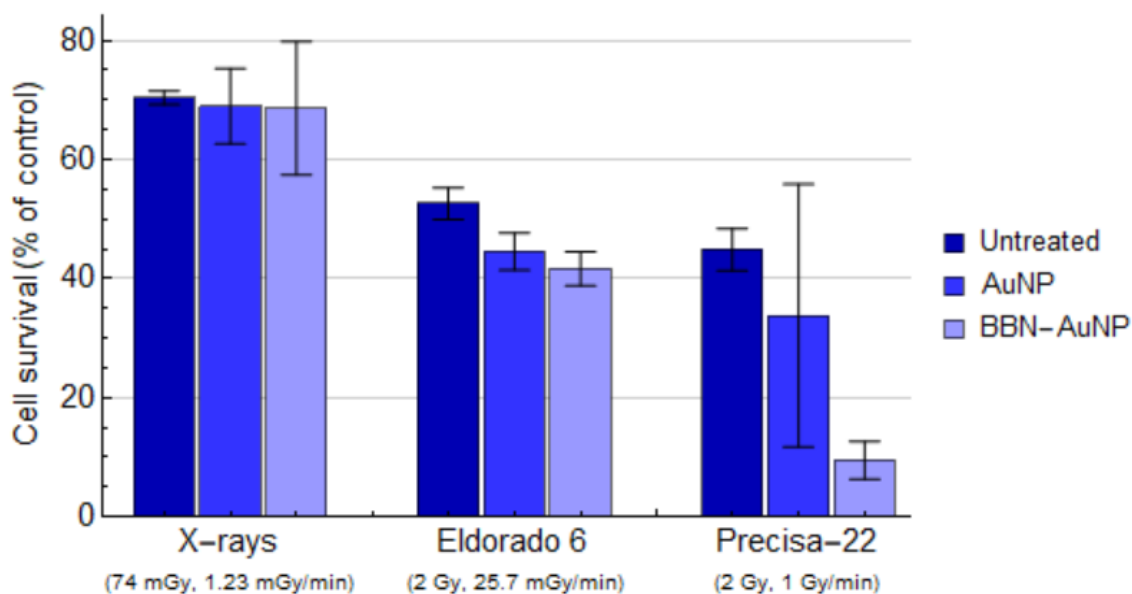


Figure 5.13: Cell survival as a percentage of each control.

The effect of the irradiation remains as expected. For the X-ray irradiation, with the lowest dose in the cells, the survival of the PC3 cells is higher (approximately 70%). In the samples irradiated with Co-60 gamma rays, the total dose incident in the cells was higher and the survival fraction of the PC3 cells was around 50%.

It is possible to see that for the X-rays irradiation, the effect of the NPs has disappeared. The cell survival stayed constant independently of the initial incubation with AuNPs or BBN-AuNPs. For the irradiations with Co-60 gamma rays, although the variation between AuNPs and BBN-AuNPs is not significant, a difference can be seen between the cells without NPs and the samples with BBN-AuNPs. With Eldorado 6, there was a decrease of the survival fraction of $(21 \pm 7)\%$ in the cells with BBN-AuNPs. With Precisa-22, this decrease was of $(79 \pm 12)\%$.

In figures 5.14 and 5.15, there are photos of the clonogenic assays from the Precisa-22 irradiation and the X-rays and Co-60 irradiation, respectively. The places where there were colonies were painted in the outside of the plates with a blue pen, for easier visualization. The decrease in the number of colonies is visible from the control cells to the irradiated PC3 cells and the cells with NPs in the first image and in the second, there is a lower cell survival for the samples irradiated with Co-60 gamma rays.

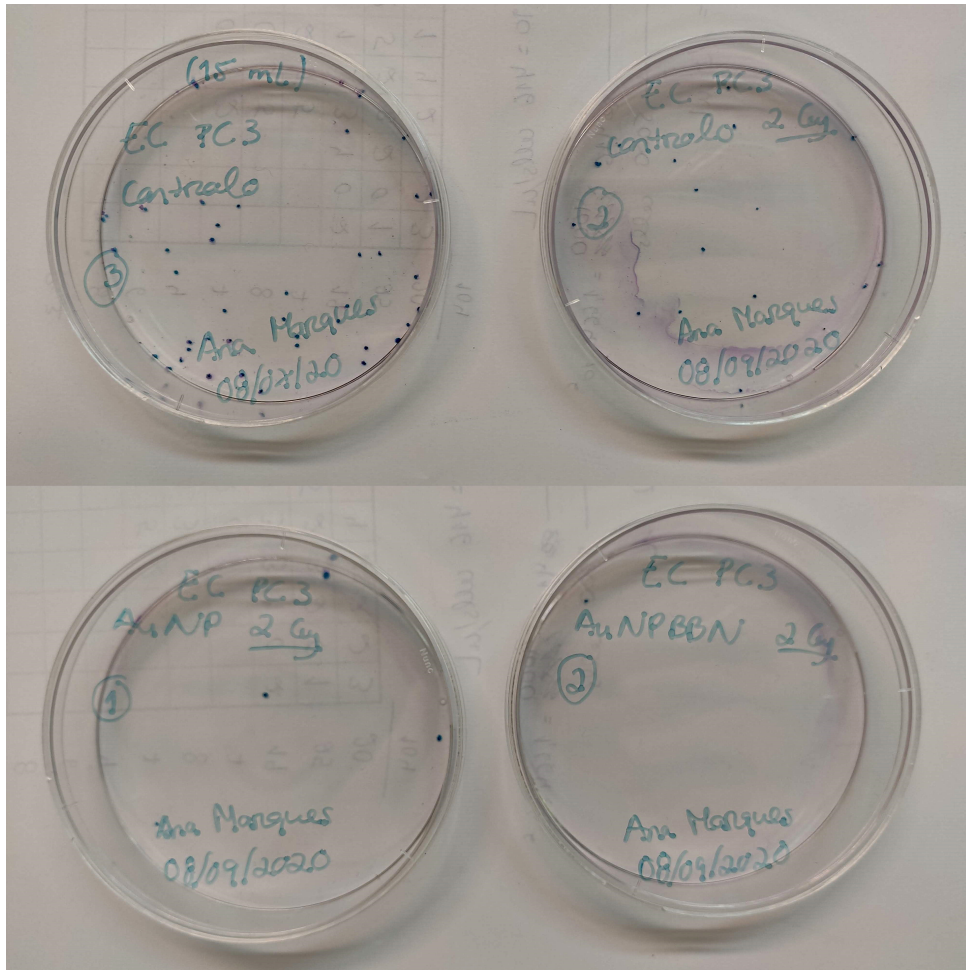


Figure 5.14: Photo of the clonogenic assay 13 days after irradiation with Precisa-22. At the top, there is on the left the control cells and on the right the irradiated PC3 cells and at the bottom, on the left the irradiated PC3 cells with AuNPs and on the right the irradiated PC3 cells with BBN-AuNPs.

5.4 Monte Carlo simulations

5.4.1 Variation of the distance between the NP and the source

The first simulation had the goal of studying the effect of the distance between the NP and the source in the DEF, as well as seeing the difference between X-ray and Co-60 irradiations. The distances ranged from $1 \mu\text{m}$ to 1 cm. Although in reality the distance between the source and the NP would be bigger, simulating this would lead to a very high computation time and for the purpose of this study, these distances are enough to evaluate the effect of the distance in the DEF.

It can be seen that, as expected, the DEF caused by X-rays is higher than the DEF caused by Co-60 gamma rays. In fact, the DEF after Co-60 irradiation quickly decreases to values near 1 as the distance between the source and the NP increases. These values are compatible with the results from the articles [43] and [46].

Additionally, for the distances considered, there is not a significant variation of the DEF with different distances.

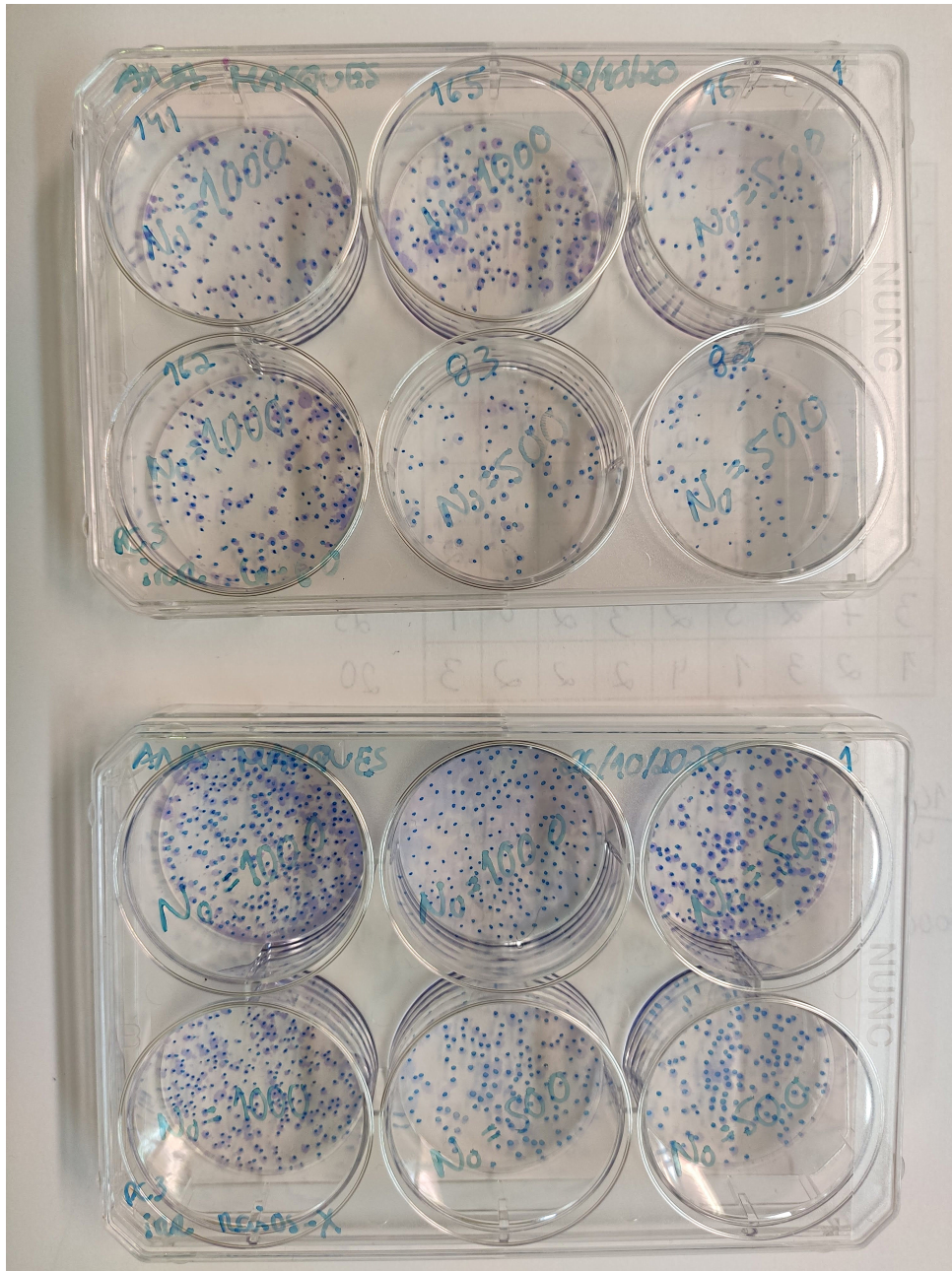


Figure 5.15: Photo of the clonogenic assay 13 days after irradiation with Eldorado 6 and X-rays. At the top, there is the plate with the PC3 cells without NPs irradiated with Co-60 gamma rays and at the bottom, PC3 cells also without NPs irradiated with X-rays.

5.4.2 Variation of the NP size

For the next simulation, the AuNP diameter was changed for three different beam widths of 50 kVp X-rays. For the beam width of 654 and 800 nm, six data points were simulated and for the smallest beam, nine data points were simulated.

It can be seen from figure 5.16 that there is a linear relation between the DEF and the volume of the NP. The slope of this curve depends on the beam width. Bigger beams have a smaller slope, showing the importance of secondary particle equilibrium.

In these simulations, it was possible to also calculate the energy deposited outside of the NP and

Distance (μm)	DEF X-rays	DEF Co-60
1	78 ± 3	2.4 ± 0.5
5×10^1	66 ± 4	1.5 ± 0.4
1×10^2	66 ± 4	1.7 ± 0.3
1×10^3	64 ± 3	1.6 ± 0.3
1×10^4	68 ± 4	1.6 ± 0.3

Table 5.1: Results on the variation of the distance between the source and the NP

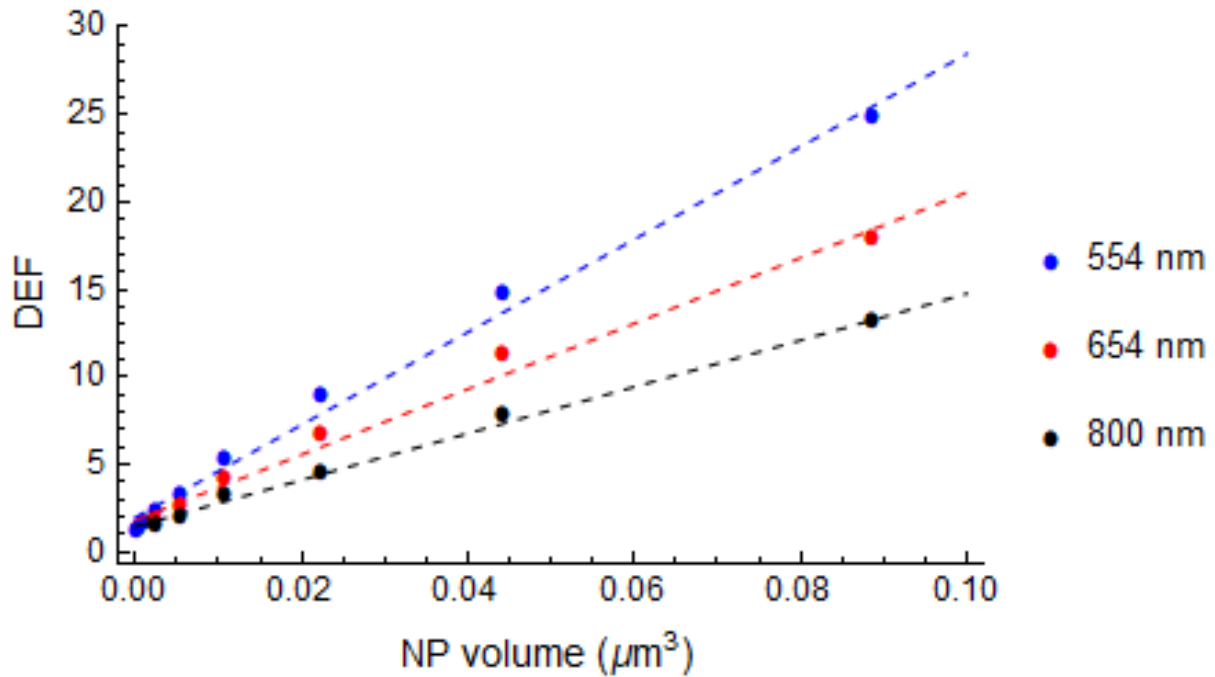


Figure 5.16: Effect of the variation of the NP size, for three different beam widths: 554, 654 and 800 nm.

relate it to the NP volume. The results are in the plot 5.17. The y-axis corresponds to the energy deposited outside of the NP divided by the sum of the energies deposited inside and outside of the NP (inside the cell).

As mentioned in section 3.2, increasing the size of the NP is going to increase the number of secondary electrons that will deposit their energy inside the NP and consequently, increase the number of secondary electrons that will not contribute to a radiosensitization effect. However despite the decreasing energy deposited in the cell, even with the biggest NP, there is still about 55 % of the total energy that is deposited outside of the NP and, as visible in figure 5.16 there is still a higher DEF for bigger NPs.

This simulation had the cell divided into nucleus and cytoplasm in order to estimate the energy deposited in these bodies. In each one, the variation of the DEF followed the same tendency as the DEF in the overall cell but the DEF in the nucleus was bigger than the DEF in the cytoplasm. This happens because the NP is placed inside the nucleus and the low-energy secondary electrons, such as Auger electrons, that escape the NP will deposit their energy in the nucleus and only the particles with

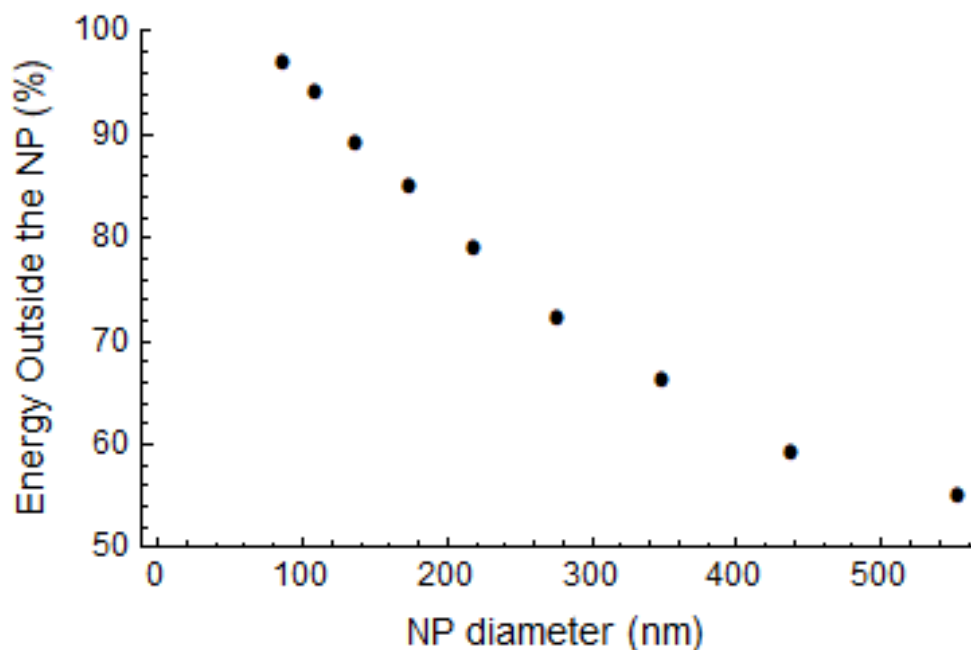


Figure 5.17: Energy deposited outside of the NP, as a fraction of the total deposited energy, for several NP sizes, for the 564 nm beam. All points had an uncertainty of 1%.

higher energy will leave the nucleus into the cytoplasm.

NP diameter (nm)	DEF nucleus	DEF cytoplasm
534	39 ± 1	9.1 ± 0.3
440	23 ± 1	5.6 ± 0.3
350	13.2 ± 0.9	3.8 ± 0.3
277	7.7 ± 0.5	2.5 ± 0.2
220	4.6 ± 0.3	1.8 ± 0.1
175	3.0 ± 0.2	1.3 ± 0.1
139	2.0 ± 0.2	1.2 ± 0.1
110	1.5 ± 0.1	1.1 ± 0.1
87	1.3 ± 0.1	1.04 ± 0.09

Table 5.2: DEF in the nucleus and in the cytoplasm with varying NP sizes.

5.4.3 Simulations with several NPs

For these simulations, the objective was to compare the DEF for 1 NP with a radius of 10 nm and for 125 NPs with a radius of 2 nm each. This DEF was calculated considering the amount of energy deposited in a 100 nm water sphere when the NPs were made of gold and water. The results gave a DEF of 2.6 ± 0.4 for the 125 NPs and 2.1 ± 0.3 for the single NP. These values are in agreement with each other, because

the uncertainty intervals overlap, and therefore it can be concluded that the DEF calculated for several smaller NPs can be approximated by the DEF for only one NP, if the bigger NP has the same volume as the summed volumes of the smaller NPs.

5.4.4 Simulations with the experimental conditions

For these simulations, the variation of the DEF with distance was studied, for two different beam widths. The parameters used are in section 4.1, but they were chosen to simulate the real setups from the X-ray irradiation and the Precisa-22 irradiator, taking into account the computational time.

The results are in figures 5.18 and 5.19 for X-rays and Co-60, respectively. The plots contain the variation of DEF with distance. While the simulation was run with the shells going from the NP to the nucleus, this is a very local effect and so, in order to see the effect better, in the plot the distances range from the NP to 1.7 μm .

In the shell immediately after the NP, as expected, is where the DEF is higher, quickly decreasing to 1 after only 500 nm. In the X-rays simulation, for a 1 μm beam, where secondary electron equilibrium does not exist, the DEF is 14 ± 2 and for a 50 μm beam, the DEF decreases to 4.6 ± 1.8 . For Co-60, also for the 1 μm , the DEF is 1.8 ± 0.4 , decreasing to 1.2 ± 0.4 for a 5 μm beam. It can be seen that, for the 5 μm beam of Co-60 gamma rays, there is no enhancement, not even in the first shell (considering however the very high uncertainties for the Co-60 simulations). However, when the energy deposited in all of the shells was summed and the dose calculated in the nucleus, there was no dose enhancement in neither one of the simulations. This is, therefore, as mentioned before, a very local effect occurring in the first few hundred nanometers from the NP.

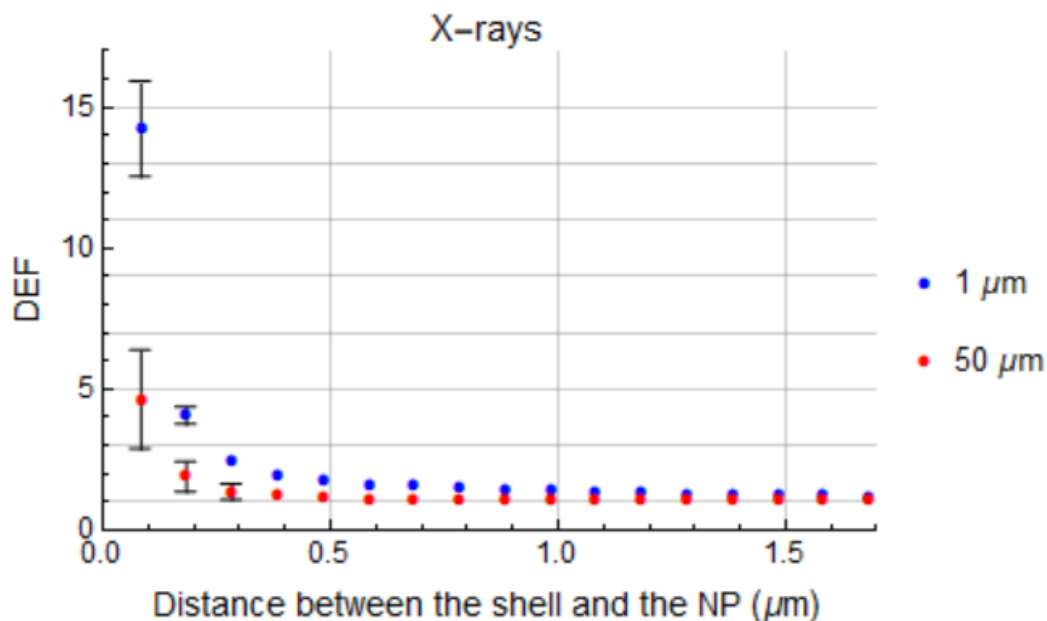


Figure 5.18: Variation of the DEF with the distance, here calculated as the distance between the inner layer of each shell and the center of the NP, for two different beam widths of 1 and 50 μm , with X-rays. Uncertainties below 5 and 20 % are not shown for the data points with the beam width of 1 and 50 μm respectively.

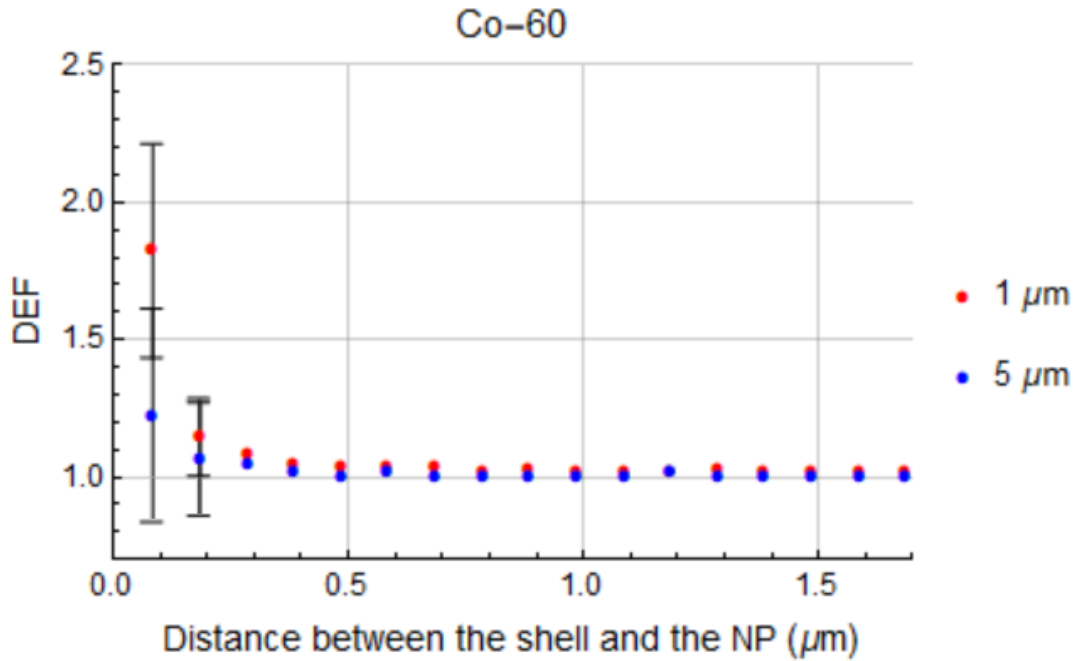


Figure 5.19: Variation of the DEF with the distance, here calculated as the distance between the inner layer of each shell and the center of the NP, for two different beam widths of 1 and 5 μm , with Co-60. Uncertainties below 10 and 15 % are not shown for the data points with the beam width of 1 and 50 μm respectively.

Additionally, the energy deposited on the first and second shells per particle type was recorded, for the simulations with gold and water, for the 1 μm beam. For the other beam widths, this was only recorded for the first shell. In table 5.3, these results are presented for electrons as the ratio between the energy deposited in each shell for gold and for water. For photons, this ratio is approximately 1 in both simulations. It can be seen that the ratio in the energies deposited by electrons is higher for X-rays, confirming that the dose enhancement is caused by the low-range Auger electrons. Furthermore, as expected, the DEF in the Co-60 simulations is very close to 1.

Shell	Beam	Energy ratio X-rays	Energy ratio Co-60
1	Small	11.8 ± 0.4	1.18 ± 0.08
	Large	3.3 ± 0.4	1.0 ± 0.1
2	Small	4.5 ± 0.2	1.1 ± 0.1

Table 5.3: Ratio between the energy deposited by electrons on each shell for the gold simulation and the water simulation. The small beam corresponds to a width of 1 μm and the large beam to a width of 5 and 50 μm for Co-60 and X-rays, respectively.

Chapter 6

Discussion and Conclusions

In this chapter, the results presented previously are discussed and compared, both experimental and computational. In the end, there is a brief conclusion of the thesis and ideas for future work.

6.1 Discussion of results

In the following subsections, there are several comparisons that could be made from the experimental and computational results. It is important to mention that this work was affected by the pandemic. It was not possible to perform more assays, for example, to calculate or reduce uncertainties in the results. This is visible in sections 5.2.1 and 5.2.2, where the dose point for 4 Gy does not have an associated uncertainty, as this was only performed once. In the CBMN assays with nanoparticles, it was also not possible to calculate the uncertainties due to these time constraints. In the MTT assays, mostly in the Precisa-22 irradiations, an extra assay would have been ideal to decrease the uncertainties in the cellular viability. In the clonogenic assay, an extra assay for the X-rays irradiation would also be ideal, as well as in Precisa-22 because there was an unusually high variation of the cell survival values in the cells incubated with AuNPs (from figure 5.13). All of these situations occurred not only due to the pandemic but also because there was a limited amount of NPs available for this thesis.

6.1.1 Comparison between Co-60 gamma rays and X-rays

The first section of this discussion compares two different types of radiation, i.e. Co-60 gamma rays and X-rays. It is important to note that, besides the different energies, both the dose rate and the total dose are different in the two cases, as mentioned in section 3.7. Nonetheless some comparisons can be made.

The damages in the cells one day after the irradiation are visible in the CBMN assay. In figure 5.6, it can be seen that for the cells without NPs, there are more micronuclei in binucleated cells for gamma rays than for X-rays and this tendency is maintained for the cells with AuNPs. However, in the cells with BBN-AuNP, there are less micronuclei in the Eldorado 6 irradiator, followed by X-rays and finally by the Precisa-22 irradiator. From this plot alone, the X-rays seem a better option for treatment with

AuNPs because its effects are similar to those of gamma rays, but the total dose in the cells is much lower. However, in figure 5.9, the percentage of binucleated cells with more than one micronucleus is plotted. Here, it is visible that the damages caused by gamma rays are harder to repair, i.e. the sum of all the micronuclei in the binucleated cells might be similar for X-rays and gamma rays, but for gamma rays there are more clustered damages inside the cells. Therefore, with X-rays, the cancer cells might be able to repair themselves and these damages might not necessarily lead to cell death, making the treatment ineffective.

The MTT assay can give an idea on the cellular viability after three days. In this period of time, approximately three cellular divisions have occurred and some damages were repaired. It can be seen in figure 5.11 that the cellular viability for the cells without NPs is similar in all three sources considering the uncertainty intervals, however this result for the Eldorado 6 irradiator is around 100% viability, $(99 \pm 5)\%$, indicating that almost all damages were repaired. For X-rays this value was slightly inferior, $(80 \pm 12)\%$. Regarding the effect of the NPs, it is very significant for the gamma rays in Eldorado 6 but for Precisa-22 the uncertainty intervals are too large for a conclusion to be made, as well as for the X-rays. Nonetheless, the decrease in cellular viability with the NPs is close for both X-rays and gamma rays, even though once again the dose in the cells irradiated with X-rays is much lower.

Finally the clonogenic assay allows for the estimation of cell survival after several days, in this case, thirteen days. From figure 5.13, the cells under X-ray irradiation were the cells with the highest survival with values very close to those in the MTT assay. From this plot, the Co-60 gamma rays were the ones that caused more damages that, in the long term, caused cell death.

In conclusion, the effects caused by the NPs in the cells a few days after the irradiation are similar for X-rays and Co-60 gamma rays even if the total dose with X-rays was only 74 mGy and with gamma rays was 2 Gy. Therefore, in short term, X-rays would be a better option for treatment. To produce the same effects as the irradiation with X-rays, the dose in the cells with Co-60 gamma rays has to be higher, also increasing the dose in the surrounding healthy tissues. However, in long term, the damages caused by the X-rays irradiation are more easily repaired by the cells. This suggests that using X-rays could not only be ineffective in killing the tumour cells, at least for the dose used here, but also the effect of the addition of the NPs is not significant and, therefore, there would be no advantage in its use. Nonetheless, because there are effectively damages in the nucleus of the cells in the first days, a good option would be to increase the total dose in the cells or to perform a treatment with dose fractionation. This would not only give the healthy cells around the tumour a higher chance of repairing their damages, but also create more clustered damages in the cancer cells. In long term, the Co-60 gamma rays prove to be a better treatment option, as they lead to a smaller cell survival in figure 5.13, for the doses used.

Even though, physically, the effect occurs only for X-rays irradiation, it can be seen in these results that there is an effect even with Co-60 irradiation that cannot be explained by the different mass-energy absorption coefficients for gold and water as for X-rays. The effect still occurs, most likely, due to ROS production, as mentioned in section 2.6.

6.1.2 Comparison between AuNPs and BBN-AuNPs

From the CBMN assay, in figure 5.6, there is a significant difference in the micronuclei yield when comparing the PC3 cells incubated with AuNPs and BBN-AuNPs, for both X-rays and Co-60 gamma rays from Precisa-22. In the plot with the cells with more than one micronuclei, the effect is only visible for Precisa-22. Accordingly it can be concluded that one day after the irradiation, there is an increased radiosensitization effect of the BBN-AuNPs compared to that of the AuNPs in the PC3 cells, for two of the three irradiation sources studied, as this difference does not occur in the Eldorado 6 irradiator.

Two days later, in the MTT assay, there is still no significant difference for the cells irradiated with the Eldorado 6. With the other sources, this difference is small considering the uncertainties. With Precisa-22, the cellular viability relative to the control was $(93 \pm 15)\%$ and $(61 \pm 13)\%$ with AuNPs and BBN-AuNPs, respectively. With X-rays, the viability decreased from $(76 \pm 7)\%$ to $(61 \pm 1)\%$ when the cells were previously incubated with BBN-AuNPs instead of AuNPs. Therefore, once again there is indeed a higher dose enhancement effect with BBN-AuNPs in two of three radiation sources, even three days after the irradiation.

In the last assay, there is no significant difference in the cell survival between the cells incubated with AuNPs and BBN-AuNPs in all three sources, although the irradiated cells with AuNPs in Precisa-22 show a very high variation of the survival results, leading to a very high uncertainty in this value. If the uncertainty was of the same order as the other values from Precisa-22, there could be a distinction between the results from the use of AuNPs and BBN-AuNPs not visible here. Consequently, it can be concluded that thirteen days after the irradiation, the higher number of damages in the cells seen from the CBMN assay in the samples with BBN-AuNPs disappears, as the damages were repaired by the cells.

In short, there is in fact a higher radiosensitization effect when BBN-AuNPs are used, because their uptake into the cells is higher, however this effect increases the damages inside the cells only in a few days after the irradiation. After a longer period of time, there is no difference in the cell survival between the cells with AuNPs and the cells with BBN-AuNPs.

6.1.3 Comparison between dose rates

As mentioned in section 3.3, the Precisa-22 irradiations were performed at a dose rate of 1 Gy/min, while with the Eldorado 6 irradiator, a dose rate of 25.7 mGy/min was used. The cells received the same total dose and therefore, the results can be directly compared.

In the CBMN assay, the micronuclei yield in binucleated cells is higher in the cells incubated with BBN-AuNPs for the highest dose rate, however it is lower for this dose rate when they are incubated with AuNPs. When looking at figure 5.9, it can be seen that as expected the number of cells with more than one micronuclei is higher for the irradiation with a higher dose rate, making the damages harder for the cell to repair.

From the MTT assay, the results are very similar between the two dose rates, in the cells without NPs, with AuNPs and with BBN-AuNPs. With the lowest dose rate the difference between the cells without

NPs and with BBN-AuNPs is much more evident, because the uncertainties are higher for the irradiation with the highest dose rate, however the uncertainty intervals of both results intersect. Exemplifying, when the cells with BBN-AuNPs were irradiated with the highest dose rate the decrease in the cellular viability was around $(33 \pm 21)\%$ and the ones irradiated with the lowest dose rate had a decrease in the cellular viability of $(27 \pm 5)\%$.

In the clonogenic assay, the effect of the BBN-AuNPs is very pronounced in the irradiation with Precisa-22, at the highest dose rate, however there is still a decrease in the cell survival for the Eldorado 6 irradiations when the cells were incubated with BBN-AuNPs. At the lowest dose rate, the decrease in the cell survival was of $(21 \pm 7)\%$ and with the highest dose rate this value increased to $(79 \pm 12)\%$.

To summarize, the radiosensitization effect of the BBN-AuNPs is increased when a high dose rate of Co-60 gamma rays was used, in comparison to a low dose rate of the same radiation. This becomes more evident as time passes after the irradiation because a high dose rate will create more clustered damages in the cells, which are harder to repair. It is evident from these results that, when studying the dose enhancement caused by NPs, the dose rate is a parameter just as important as the total dose in the cells.

6.2 Comparison between experimental and computational work

The simulations performed with PENELOPE do not take into account the repair of damages in the cell. Therefore, it is more accurate to compare the simulation results only with the CBMN assay. Furthermore, in the simulations, the NP was placed in the nucleus and its size was chosen so that the concentration of gold in the cells was approximately the same as the one used in the experiments. This means that for the simulations, it was assumed that there was a cellular uptake of 100 %. Therefore, the simulation results will be compared with the experimental results using the BBN-AuNPs because, in principal, its cellular uptake is higher than that of AuNPs. The Co-60 irradiations will be compared with the Precisa-22 results, because the parameters were adjusted to this irradiator. The spectra used in both situations, Co-60 and X-rays, was approximately the same between the simulations and experimental procedures. The concentration of NPs used in the simulations was $37.5 \mu\text{g/mL}$ while the experimental one was $36 \mu\text{g/mL}$.

For X-rays the experiments showed that the irradiated cells with BBN-AuNPs had 3 times more damages than the cells with BBN-AuNPs that were not irradiated and 1.2 times more damages than in the irradiated untreated PC3 cells. On the other hand, the simulated DEF was 4.6 ± 1.8 in the first shell after the NP for the largest beam. It is hard to compare the computational results with the experimental ones. They cannot be compared directly because there were a few approximations used in the simulations that affect the results, the biggest being the NP itself. While it was proved from the results in section 5.4.3 that using several NPs or one bigger NP does not significantly alter the DEF, it cannot be concluded that, biologically, having one bigger NP or a lot of smaller ones causes the same damages. Other major differences between the experiment and the simulations are the cellular uptake and the distribution of the NPs in the cell. In the simulations, it was assumed that the concentration of gold inside the cell was

37.5 $\mu\text{g/mL}$, but in reality, not all of the NPs will enter the cell and cause the dose enhancement. Then in the experiments, the actual concentration of gold inside the cells is lower and therefore the DEF is expected to be smaller than in the simulations. Finally, in the simulations, all of the NPs were placed inside the nucleus, which will cause the DEF to be higher in the nucleus. However in the experiments, the NPs inside the cells are not entirely in the nucleus, they will also appear in the cytoplasm. Most of the Auger electrons created from the interaction of the radiation with these NPs located in the cytoplasm will not reach the nucleus and cause nuclear damage, which is what is assessed by the CBMN assay. Therefore, in the experiments, there are going to be less damages in the nucleus than the damages that the simulated DEF could indicate. This is another reason to explain the higher DEF in the simulations.

For Co-60, in the experimental part, the irradiated cells with BBN-AuNPs had almost 3.5 times more damages than the cells with BBN-AuNPs that were not irradiated and 1.5 times more damages than in the irradiated untreated PC3 cells. In the simulation, the DEF obtained with the largest beam was 1.2 ± 0.4 in the first shell around the NP, indicating that there was no radiosensitization effect. Although these results are very different from each other, it is what was expected, because the effect caused by the NPs after Co-60 irradiation cannot be explained by the physical interaction of the photons with the cells, but instead they are based on the chemical reactions happening after the initial ionizations, which the software used does not compute.

Overall these simulations give a general idea of how certain parameters influence the dose enhancement effect, such as the NP size and type of radiation, but cannot yet provide an estimation of the value of the DEF. For this, a better option would be, for example, to use Geant4-DNA, which also contains processes for the modeling of biological damage induced by ionising radiation at the DNA scale.

6.3 Conclusions

This thesis had the objective of studying the radiosensitization effect of AuNPs in PC3 cells. This was achieved through in vitro assays as well as Monte Carlo simulations.

According to the obtained simulation results, there is a radiosensitization effect caused by the difference in the mass-absorption coefficients of gold and water and therefore depending on the energy of the incident photons. This effect is higher for keV energies and lower for MeV energies, such as the energies of Co-60 gamma rays, as verified in the simulation results. For a NP with a diameter of 100 nm and a beam width of 110 nm, the values of the DEF were around 70 for X-rays and 2 for Co-60, in a 1 μm shell around the NP. These values are however overestimated, because there was no secondary particle equilibrium with the chosen beam widths.

When performing simulations with approximate parameters as the experimental irradiations, the results gave a DEF of around 5 for X-rays and 1 for Co-60, in a 100 nm shell immediately after the NP, proving again the difference between the two type of radiations. These results are, however, hard to compare to the experimental values obtained due to the several approximations/limitations in the simulations.

The experimental part of the thesis involved three different assays, in order to evaluate this effect

one, three and thirteen days after the irradiation. It was concluded that BBN-AuNPs show a higher dose enhancement effect than simple AuNPs. Furthermore, a small dose of 74 mGy in the cells, from X-ray irradiation, led to a significant radiosensitization effect in short term, however after thirteen days had passed, the effect was no longer visible. For Co-60 irradiation, it was concluded that a high dose rate improved the dose enhancement from the NPs and that the effect occurred even after the thirteen days for this high dose rate. An MTT assay of RWPE-1 cells after irradiation with Precisa-22 proved the low radiosensitization effect in normal healthy cells due to the low number of receptors in these cells' membranes and consequently the low concentration of NPs inside them.

6.4 Future Work

Regarding the computational work, a few ideas for future improvement are:

- Using different Monte Carlo codes to compare the results of the simulations, such as Geant4 or MCNP;
- Using a Monte Carlo software that also simulates the production of ROS, in order to have a more realistic value of the DEF, specially for Co-60 irradiations;
- Including different distributions of the AuNPs in the cells and not adding them only to the nucleus;
- Studying the radiosensitization effect of AuNPs for different peak energies of X-rays and the variation of the DEF with this parameter.

In the experimental field, it would be interesting to:

- Perform the same assays for healthy prostate cell lines, such as RWPE-1, and effectively check that even after some time the radiosensitization effect in these cells is smaller due to the lower number of receptors in their membranes and consequently the lower uptake of NPs into the cells;
- Study the effect of different X-ray peak energies on the dose enhancement;
- Perform these experiments for the same total dose in the cells for X-rays and Co-60 gamma rays;
- Study the effect of dose fractionation in the radiosensitization of the NPs;
- Evaluate mitochondrial damages caused by NPs, as these can also lead to cell death;
- Study this effect for different particle beams, such as electron or proton beams.

Bibliography

- [1] World Health Organization. Cancer. <https://www.who.int/news-room/fact-sheets/detail/cancer>, 2018. [Online; accessed 23-November-2019].
- [2] Pordata. Óbitos por algumas causas de morte (%). [https://www.pordata.pt/Portugal/%D3bitos+por+algumas+causas+de+morte+\(percentagem\)-758-235710](https://www.pordata.pt/Portugal/%D3bitos+por+algumas+causas+de+morte+(percentagem)-758-235710), 2019. [Online; accessed 24-November-2019].
- [3] World Cancer Research Fund. Prostate cancer statistics. <https://www.wcrf.org/dietandcancer/cancer-trends/prostate-cancer-statistics>. [Online; accessed 24-November-2019].
- [4] S. Rehman. *An Overview of Cancer Treatment Modalities*. 09 2018. ISBN 978-1-78923-777-1. doi: 10.5772/intechopen.76558.
- [5] K. Haume, S. Rosa, S. Grellet, M. Śmiałek, K. Butterworth, A. Solov'yov, K. Prise, J. Golding, and N. Mason. Gold nanoparticles for cancer radiotherapy: a review. *Cancer Nanotechnology*, 7:8, 11 2016. doi: 10.1186/s12645-016-0021-x.
- [6] S. Rosa, C. Connolly, G. Schettino, K. Butterworth, and K. Prise. Biological mechanisms of gold nanoparticle radiosensitization. *Cancer Nanotechnology*, 8, 12 2017. doi: 10.1186/s12645-017-0026-0.
- [7] L. E. Rosenberg and D. D. Rosenberg. Chapter 16 - the genetics of cancer. In L. E. Rosenberg and D. D. Rosenberg, editors, *Human Genes and Genomes*, pages 259 – 288. Academic Press, San Diego, 2012. doi: <https://doi.org/10.1016/B978-0-12-385212-0.00016-0>. URL <http://www.sciencedirect.com/science/article/pii/B9780123852120000160>.
- [8] Z. Abbas and S. Rehman. *An Overview of Cancer Treatment Modalities*. 09 2018. doi: 10.5772/intechopen.76558.
- [9] B. S.-G. J. L. A. T. M. V. Manuel Arruebo, Nuria Vilaboa and África González-Fernández. Assessment of the evolution of cancer treatment therapies. *Cancers*, 3:3279–3330, 2011. doi: 10.3390/cancers3033279.
- [10] J. Skowronek. Current status of brachytherapy in cancer treatment - short overview. *Journal of contemporary brachytherapy*, 9:581–589, 2017. doi: 10.5114/jcb.2017.72607.

- [11] T. M. Royce TJ, Qureshi MM. Radiotherapy utilization and fractionation patterns during the first course of cancer treatment in the united states from 2004 to 2014. *Journal of the American College of Radiology*, 15:1558–1564, 2018.
- [12] E. Hall and A. Giaccia. *Radiobiology for the Radiologist*. Wolters Kluwer Health, 2018. ISBN 9781496395139. URL <https://books.google.pt/books?id=rcNVDwAAQBAJ>.
- [13] C. Theodorakis. *Mutagenesis*, pages 2475–2484. 01 2008. doi: 10.13140/2.1.4219.9688.
- [14] T. Kim, K. Lee, Seo, Kang, Seong, and Youn. Cellular stress responses in radiotherapy. *Cells*, 8: 1105, 09 2019. doi: 10.3390/cells8091105.
- [15] M. S. D’Arcy. Cell death: a review of the major forms of apoptosis, necrosis and autophagy. *Cell Biology International*, 43(6):582–592, 2019. doi: 10.1002/cbin.11137. Available at <https://onlinelibrary.wiley.com/doi/abs/10.1002/cbin.11137>.
- [16] Kim, W. et al. Cellular stress responses in radiotherapy. *Cells*, 8:1105, 09 2019. doi: 10.3390/cells8091105.
- [17] *Gamma- and X-Ray Interactions in Matter*, chapter 7, pages 124–159. John Wiley & Sons, Ltd, 2007. ISBN 9783527617135. Available at <https://onlinelibrary.wiley.com/doi/abs/10.1002/9783527617135.ch7>.
- [18] J. Turner. *Chemical and Biological Effects of Radiation*, chapter 13, pages 399–447. John Wiley & Sons, Ltd, 2007. ISBN 9783527616978. doi: 10.1002/9783527616978.ch13. Available at <https://onlinelibrary.wiley.com/doi/abs/10.1002/9783527616978.ch13>.
- [19] G. R. CHOPPIN, J.-O. LILJENZIN, and J. RYDBERG. Chapter 6 - absorption of nuclear radiation. In G. R. CHOPPIN, J.-O. LILJENZIN, and J. RYDBERG, editors, *Radiochemistry and Nuclear Chemistry (Third Edition)*, pages 123 – 165. Butterworth-Heinemann, Woburn, third edition edition, 2002. ISBN 978-0-7506-7463-8. doi: <https://doi.org/10.1016/B978-075067463-8/50006-6>. URL <http://www.sciencedirect.com/science/article/pii/B9780750674638500066>.
- [20] Z. Kuncic and S. Lacombe. Nanoparticle radio-enhancement: principles, progress and application to cancer treatment. *Physics in Medicine & Biology*, 63(2), jan 2018. doi: 10.1088/1361-6560/aa99ce.
- [21] H. Byrne, Y. Gholami, and Z. Kuncic. Impact of fluorescence emission from gold atoms on surrounding biological tissue - implications for nanoparticle radio-enhancement. *Physics in medicine and biology*, 62, 02 2017. doi: 10.1088/1361-6560/aa6233.
- [22] V. Stumpf, K. Gokhberg, and L. Cederbaum. The role of metal ions in x-ray induced photochemistry. *Nature Chemistry*, 8, 05 2015. doi: 10.1038/nchem.2429.
- [23] R. Jenkins, R. Gould, and D. Gedcke. *Quantitative X-Ray Spectrometry, Second Edition*, volume 20 of *Practical Spectroscopy*. Marcel Dekker, New York, 1995.

- [24] D. YILMAZ, Y. ŞAİN, and L. DEMİR. Studies on mass attenuation coefficient, mass energy absorption coefficient, and kerma for Fe alloys at photon energies of 17.44 to 51.70 keV. *Turkish Journal of Physics*, 39:81–90, 2015. doi: 10.3906/fiz-1408-4.
- [25] A. De Angelis and M. Pimenta. *Introduction to Particle and Astroparticle Physics: Multimessenger Astronomy and its Particle Physics Foundations*. Undergraduate Lecture Notes in Physics. Springer International Publishing, 2018. ISBN 9783319781815. URL <https://books.google.pt/books?id=9upgDwAAQBAJ>.
- [26] E. Dreaden, M. Mackey, X. Huang, B. Kang, and M. El-Sayed. Beating cancer in multiple ways using nanogold. *Chemical Society reviews*, 40:3391–404, 07 2011. doi: 10.1039/c0cs00180e.
- [27] A. Araneda. *Development of a Methodology for the Determination of a TXRF Spectrometer Sensitivity Curve*. PhD thesis, 04 2015.
- [28] B. J. Choi, K. O. Jung, E. E. Graves, and G. Pratz. A gold nanoparticle system for the enhancement of radiotherapy and simultaneous monitoring of reactive-oxygen-species formation. *Nanotechnology*, 29(50):504001, oct 2018. doi: 10.1088/1361-6528/aae272. Available at <https://doi.org/10.1088>
- [29] R. Dayal, A. Singh, A. Pandey, and K. Mishra. Reactive oxygen species as mediator of tumor radiosensitivity. *Journal of cancer research and therapeutics*, 10:811–8, 10 2014. doi: 10.4103/0973-1482.146073.
- [30] Thermo Fisher Scientific Inc. *Cell Culture Basics Handbook*. 2015. Available at <https://www.thermofisher.com/content/dam/LifeTech/Documents/PDFs/PG1563-PJT1267-COL31122-Gibco-Cell-Culture-Basics-Handbook-Global-FLR.pdf>.
- [31] Tai S, Sun Y, Squires JM, et al. PC3 is a cell line characteristic of prostatic small cell carcinoma. *Prostate*, 15:1668–1679, 2011. doi: 10.1002/pros.21383.
- [32] ATCC. Cells and microorganisms. https://www.lgcstandards-atcc.org/Products/Cells_and_Microorganisms.aspx. [Online; accessed 20-August-2020].
- [33] R. Markwalder and J. C. Reubi. Gastrin-releasing peptide receptors in the human prostate. *Cancer Research*, 59(5):1152–1159, 1999. URL <https://cancerres.aacrjournals.org/content/59/5/1152>.
- [34] F. Silva. *Gallium Compounds for the Design of (Nano)radiopharmaceuticals*. PhD thesis, Faculdade de Ciências da Universidade de Lisboa, 2014.
- [35] *Ionization Chambers and Diode Detectors*. IBA Dosimetry, 2015. Available at <https://stratecservices.nl/wp-content/uploads/2015/01/Detectors.pdf>.
- [36] J. A. Seibert. X-ray imaging physics for nuclear medicine technologists. part 1: Basic principles of x-ray production. *Journal of Nuclear Medicine Technology*, 32:139–147, 2004.

- [37] B. Oorschot, S. Hovingh, H. Rodermond, A. Güçlü, N. Losekoot, A. Geldof, G. Barendsen, L. Stalpers, and N. Franken. Decay of γ -h2ax foci correlates with potentially lethal damage repair in prostate cancer cells. *Oncology reports*, 29, 03 2013. doi: 10.3892/or.2013.2364.
- [38] Fenech, Michael. Cytokinesis-block micronucleus cytome assay. *Nature Protocols*, 2:1084–1104, 05 2007. doi: 10.1038/nprot.2007.77.
- [39] V. Patravale, P. Dandekar, and R. Jain. 4 - nanotoxicology: evaluating toxicity potential of drug-nanoparticles. In V. Patravale, P. Dandekar, and R. Jain, editors, *Nanoparticulate Drug Delivery*, Woodhead Publishing Series in Biomedicine, pages 123 – 155. Woodhead Publishing, 2012. ISBN 978-1-907568-98-5. doi: <https://doi.org/10.1533/9781908818195.123>. URL <http://www.sciencedirect.com/science/article/pii/B9781907568985500048>.
- [40] G. Fotakis and J. A. Timbrell. In vitro cytotoxicity assays: Comparison of ldh, neutral red, mtt and protein assay in hepatoma cell lines following exposure to cadmium chloride. *Toxicology Letters*, 160(2):171 – 177, 2006. ISSN 0378-4274. doi: <https://doi.org/10.1016/j.toxlet.2005.07.001>. URL <http://www.sciencedirect.com/science/article/pii/S0378427405001967>.
- [41] J. Sempau, A. Badal, and L. Brualla. A PENELOPE-based system for the automated Monte Carlo simulation of clinacs and voxelized geometries—application to far-from-axis fields. *Med. Phys.*, 38: 5887 – 5895, 2011. Available at <http://dx.doi.org/10.1118/1.3643029>.
- [42] *MATLAB version 9.3.0.713579 (R2017b)*. The Mathworks, Inc., Natick, Massachusetts, 2017.
- [43] M. K. K. Leung, J. C. L. Chow, B. D. Chithrani, M. J. G. Lee, B. Oms, and D. A. Jaffray. Irradiation of gold nanoparticles by x-rays: Monte carlo simulation of dose enhancements and the spatial properties of the secondary electrons production. *Medical Physics*, 38(2):624–631, 2011. doi: 10.1118/1.3539623. Available at <https://aapm.onlinelibrary.wiley.com/doi/abs/10.1118/1.3539623>.
- [44] G. Poludniowski, G. Landry, F. DeBlois, P. M. Evans, and F. Verhaegen. SpekCalc: a program to calculate photon spectra from tungsten anode x-ray tubes. *Physics in Medicine and Biology*, 54 (19):N433–N438, sep 2009. doi: 10.1088/0031-9155/54/19/n01.
- [45] G. J. C. Michael C. Kolios. High frequency ultrasound scattering from mixtures of two different cells lines: Tissue characterization insights. *Physics Publications and Research*, 11, 2008.
- [46] W. B. Li et al. Intercomparison of dose enhancement ratio and secondary electron spectra for gold nanoparticles irradiated by X-rays calculated using multiple Monte Carlo simulation codes . *Physica Medica: European Journal of Medical Physics*, 69:147 – 163, 2020. doi: 10.1016/j.ejmp.2019.12.011.